8-2016

Tellurite Fiber for High Power Mid-Wave Infrared Supercontinuum Generation

Christopher David Dunn
Clemson University, chris29803@gmail.com

Tellurite Fiber for High Power Mid-Wave Infrared Supercontinuum Generation

---

A Thesis
Presented to
the Graduate School of
Clemson University

In Partial Fulfillment
of the Requirements for the Degree
Master of Science
Photonic Science and Technology

---

by
Christopher David Dunn
August 2016

Accepted by:
Dr. Liang Dong, Committee Chair
Dr. John Ballato
Dr. Lin Zhu

Abstract

Broadband, high-power, mid-infrared sources are critical for many applications. Fiber based supercontinuum generation is the optimum mid-infrared broadband source that can provide extended bandwidth and good coherence. Compared to alternatives such as fluorides and chalcogenides, tellurite fibers are more robust and can handle much higher power. Tellurite fibers also have high nonlinearity and a material zero dispersion wavelength close to 2 μm. This makes them ideal for nonlinear processes pumped by Tm-doped silica fiber lasers.

We demonstrated tellurite fibers by using a simple stack and draw process. This fabrication method requires simple setup and is easily repeatable. Due to the difficulty in producing soft glass tubes, we have drawn a stack-and-draw preform without the need for an over-clad tube. The stack-and-draw process provides several advantages over other solid and micro-structured designs. Our solid tellurite fiber design shows potential for broadband mid-infrared supercontinuum generation. We have also shown that designs with low dispersion are the key for broadband mid-infrared supercontinuum generation in tellurite fibers pumped at 2 μm.

Dedication

This thesis is dedicated to my family and friends. My parents have encouraged my interest in science and engineering and helped me emotionally and professionally along my journey. I will always say that I am a fusion of them both and I wouldn't have it any other way. My parents have been great role models and I hope one day that I can continue our family's contributions to science and engineering.

I also wouldn't be the man I am today if it wasn't for my two younger sisters. They taught me that love and compassion can be found in all walks of life and have helped me to remain humble.

Lastly, I need to thank my close friends and lab-mates for all the support and friendship I have received over these years.

Finally, I would like to dedicate this work to my professor Liang Dong. I am forever grateful for the opportunity to work under his supervision. It was not easy switching into the Photonics program but I acknowledge all the support and help he has given me to get to this point. I have learned as an engineer under his supervision and appreciate all the advice I have received.

Acknowledgments

I would first like to say thank you to Wade Hawkins and Maxwell Jones for their support in drawing my tellurite fiber. Not only are they both close friends but great engineers. Thanks for the fruitful discussions and excellent assistance.

Next I would like to thank Fanting Kong and Guancheng Gu for their valuable help with optics support. Both gentlemen are very knowledgeable and were a great resource if I ever encountered an optics related issue.

I would also like to thank Matthew Vanoverstraeten, Andrew Runnion, Camden Griggs, and Jonathan Drake. All four individuals were undergraduate students who worked under my supervision on this project and several others. I would like to thank them for their time and support.

Next I would like to thank Josh Parsons, Monica Kalichevsky-Dong, Jamie Shetzline, and Josh Furtick. All of these individuals have spent their own time to help me with my project and I thank them for it.

I would also like to thank Ron Synowicki for his valuable ellipsometry measurements of the tellurite glass. Nextly, I would like to thank John Driver and the Kigre team for the tellurite preforms they fabricated.

Lastly, I would like to thank the Reza Salem and DongFeng Liu with Thor Labs. Both individuals helped significantly with the supercontinuum generation measurement on my fiber. I have my results due to their invaluable expertise and support.

Table of Contents

List of Tables

List of Figures

Acronym List

MWIR- Mid-Wave Infrared
IRCM- Infrared Countermeasures
SCG- Supercontinuum Generation
IR- Infrared
RE- Rare Earth
QCL- Quantum Cascade Laser
OPO- Optical Parametric Oscillator
Nd:YAG- Neodymium: Yttrium Aluminum Garnet
CO_2- Carbon Dioxide
VOC- Volatile Organic Compounds
TeO_2- Tellurium Dioxide
Li_2O- Lithium Oxide
M- Modifier
ZnO- Zinc Oxide
$ZnCl_2$- Zinc Chloride
BaO- Barium Oxide
T_g- Glass Transition Temperature
DSC- Differential Scanning Calorimetry
ZDW- Zero Dispersion Wavelength
TIR- Total Internal Reflection
SM- Single Mode
T_{drop}- Drop Temperature
OD- Outer Diameter
PCF- Photonic Crytal Fiber
T_{draw}- Draw Temperature
C-C- Corner to Corner
RI- Refractive Index
Indium Antimonide- InSb
SPM- Self Phase Modulation

Chapter 1

Introduction

Mid-Wave Infrared (MWIR) sources are critical for a wide range of applications from identification of molecular species to counter measures for missile attacks [1]. Broader bandwidth and higher power are required for improved capabilities in many related applications. Infrared counter measures (IRCM) are a significant and growing area of research [2]. Currently, narrow-line-width lasers are used to disrupt missile tracking. Wave-skipping techniques continue to improve to avoid counter measures, rendering them less effective [3]. Probing of the MWIR region is also a desirable technology for sensing of chemical compounds. This application can be used for quick and accurate toxic chemical detection, combustion monitoring, and even medical sensor development for disease diagnosis and monitoring [4, 5].

There is a significant demand for broad, bright sources capable of covering the wavelength range from 2-5 μm. Supercontinuum generation (SCG) is a phenomena that has been researched extensively since its discovery in 1969 [6]. SCG is a process that produces a broadband high intensity spectrum of light from a series of nonlinear effects pumped by a narrow bandwidth laser. SCG is an encompassing solution providing good coherence, high output powers, and broadband spectral width needed

for several applications in the MWIR band. In addition to high MWIR transmission, the optical medium exhibiting SCG must have high nonlinearity and correctly designed dispersion. SCG within tellurite fibers is a promising technology to assist with countering missile attacks and compound detection.

1.1 Applications of MWIR Glasses

Study of the infrared (IR) spectrum began several hundred years ago in 1737 when Émilie du Châtelet predicted the light we know as infrared radiation [7]. Almost a century later, Macedonio Melloni created the first IR detector by developing a thermopile [8]. The thermopile was the first device of its kind and is able to convert thermal energy into electrical energy. Wartime efforts helped push the development of IR detection for active defense related applications. The first IR search and track device was developed to assist aircraft in discovery of foreign bodies up to one mile away. The next big leap for IR detection was the development of active infrared sights in 1945 for use with nighttime combat. Throughout the late 1940s to the early 1960s various discoveries were made in the private sector relating to detection of IR radiation but it wasn't until 1965 that a commercial IR device was manufactured. After this breakthrough, the IR spectrum gained further attention and research expanded.

The IR spectrum refers to the band of light from 750 nm to 1 mm. The MWIR band is more narrowly defined and describes the spectrum of light from 2.5 to 8 μm. There is a huge demand for MWIR lasers and broadband sources. One of the most desired applications for the MWIR band is utilization of the transparency within certain atmospheric windows. It was known as early as the 1960s that the atmosphere is permissive to light within the 3 - 4.5 μm band as well as the 8 - 13 μm band [see Figure 1.1] [9]. Utilizing these windows can lead to improvements in

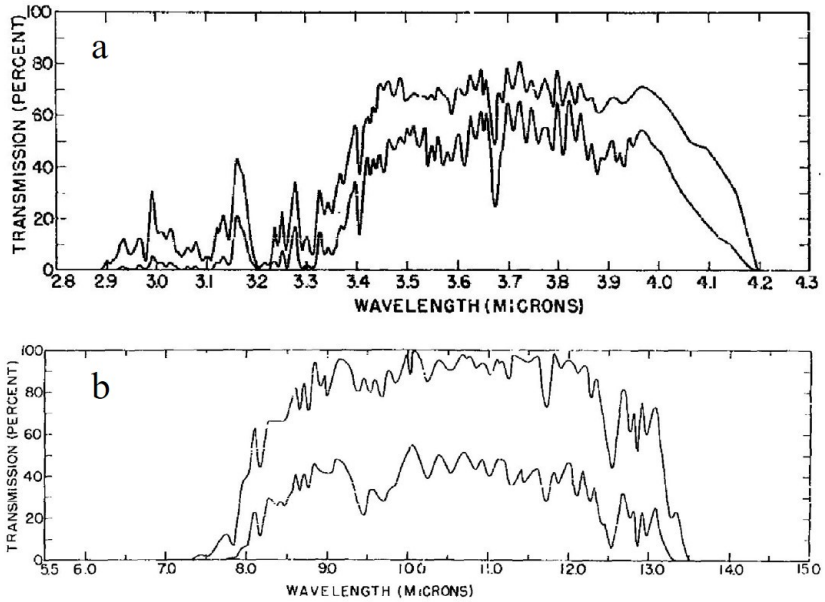

Figure 1.1: Atmospheric transmission over the Chesapeake Bay area. Tested with a 5.5 and 16.25 km path length over the: a) 2.8 - 4.3 μm range; b) 5.5 - 15.0 μm range [9].

missile defense [1].

The public sector also desires advancement in MWIR technologies. Many sensing applications hope to utilize this band for medical diagnostics, environmental monitors, and hazardous chemical detection [4]. Several of these applications require broad, bright sources that are capable of covering the MWIR spectrum. Advancements need to be made to improve upon the coverage available and to create broader sources. Supercontinuum generation in MWIR transparent fibers is a desirable solution.

Several other MWIR sources are currently available [see Figure 1.2] but do not offer the broad spectrum range and robustness that fiber based supercontinuum sources can provide. Narrow band MWIR sources include: rare earth (RE)-doped solid-state lasers, lead-salt lasers, some semi-conductor lasers, additionally limited gas and chemical lasers [10]. Although these MWIR emitting lasers are important

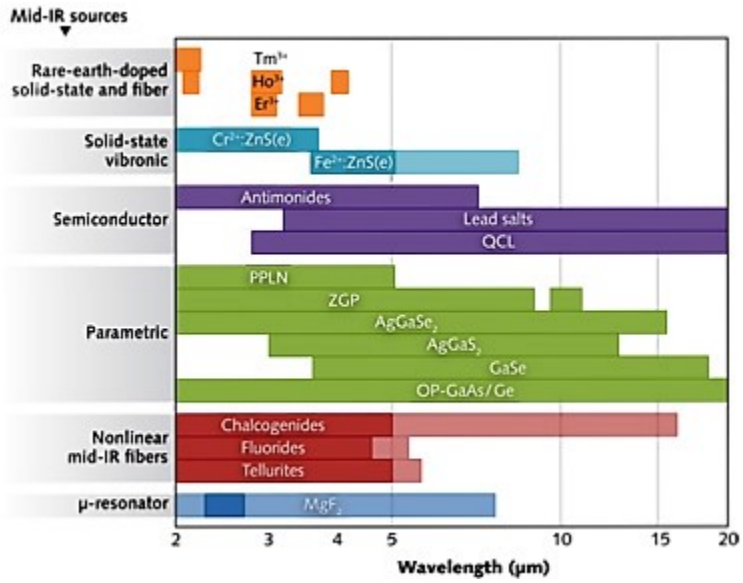

Figure 1.2: Mid-infrared sources and materials pictured with their respective wavelength ranges [10].

for several applications, we desire broadband emission that covers several microns. Currently there are multiple broadband emitting MWIR lasers in addition to the narrow band sources just mentioned. These broadband sources include: quantum cascade lasers (QCL), optical parametric oscillators (OPO), and finally SCG fiber lasers. QCL are being developed for use as a jamming device to replace tunable solid state lasers. Currently, neodymium-doped: yttrium aluminum garnet (Nd:YAG) OPO are used as a jamming device. The difference between the QCL and the Nd:YAG OPO is the QCL's ability to determine the power level and wavelengths of operation due to the flexible architecture [1]. Although these devices are useful, the broadband wavelength ranges these devices cover does not extend beyond 1 μm of spectral bandwidth. SCG has been displayed covering several microns [3, 11–13] and experimentally shown stretching between the wavelength range of 1.4 - 13.3 μm [14]. Our research indicates that moving towards a bright, broadband source such as SCG in MWIR transparent fibers will offer an encompassing solution to deter heat seeking missiles.

MWIR supercontinuum lasers can be produced from off the shelf components and will use no moving parts so they are extremely robust. The advantage of SCG over other broadband technologies is the spatial coherence of the beam and the high intensity of the output that can be compared to certain lasers. SCG is now reaching a point where expansion outside of a laboratory setting can occur due to the use of pump lasers transitioning from the large mode-locked lasers to much smaller diode lasers and fiber amplifiers. IRCM are currently deployed on all standard military aircraft. As the technology evolves, it is becoming more readily available for commercial aircrafts as well. IRCM presently involve the use of a bright illumination source such as a laser or flare that is used to confuse a heat-seeking missile's target acquisition system and direct the threat elsewhere. Although this technology is effective, target acquisition methods are being developed to bypass these counter measures therefore more robust systems need to be implemented.

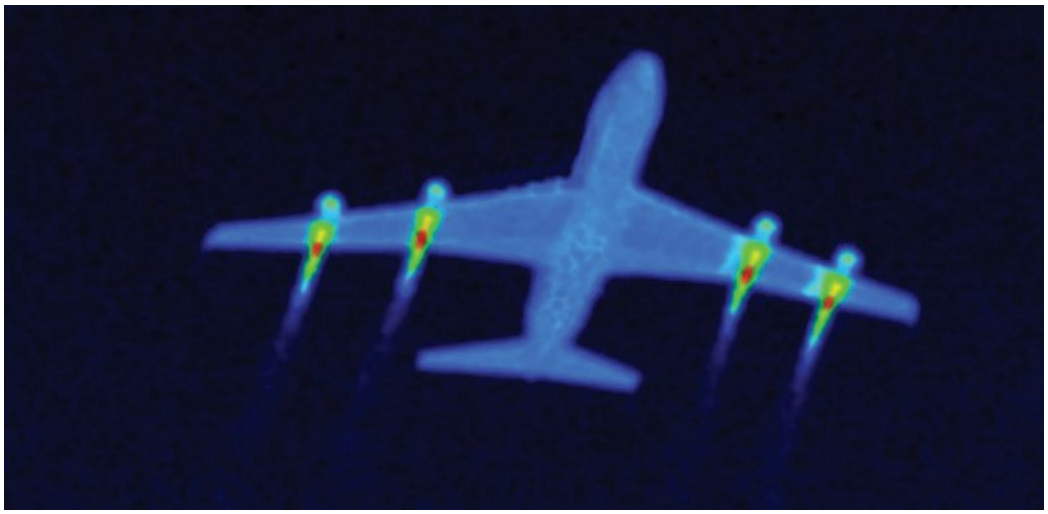

Figure 1.3: The infrared signature of a commercial aircraft in the 3-5 um band showing an easy target for heat-seeking missiles [2].

IRCM currently deployed are proprietary with their own mechanism for deterring missiles, yet all of them have the same basic functions. The main components of

an IRCM system would be the IR camera that is used to locate and track the missile, then the jammer or bright light source, mechanical components that would rotate the imager or light source, and finally the data-processing system that would be used to control the functions and be programmed for pattern recognition. A counter measure system would look similar to the device pictured in Figure 1.4 and would sit atop, below, or at the nose of an aircraft to provide full protection. The difficulty with the

Figure 1.4: Infrared counter measure systems employed on commercial and military aircrafts. The depicted models are located on the bottom of the aircraft but IRCM can be located in more than one location on the aircraft including: top, front, and back so that they may cover all areas of attack [2].

jammer would be the ability to provide a brighter modulated source that would act as deterrent in the same field of view as the aircraft. Northrop Grumman has been on the forefront of IRCM developing the first IR jamming laser, called the Viper^{TM}. The Viper^{TM} uses a Nd:YAG laser that performs constant wavelength conversions to con-

fuse the target and direct path elsewhere. While this has been very effective, missile detection advances are also increasing and determining new methods for countering these efforts.

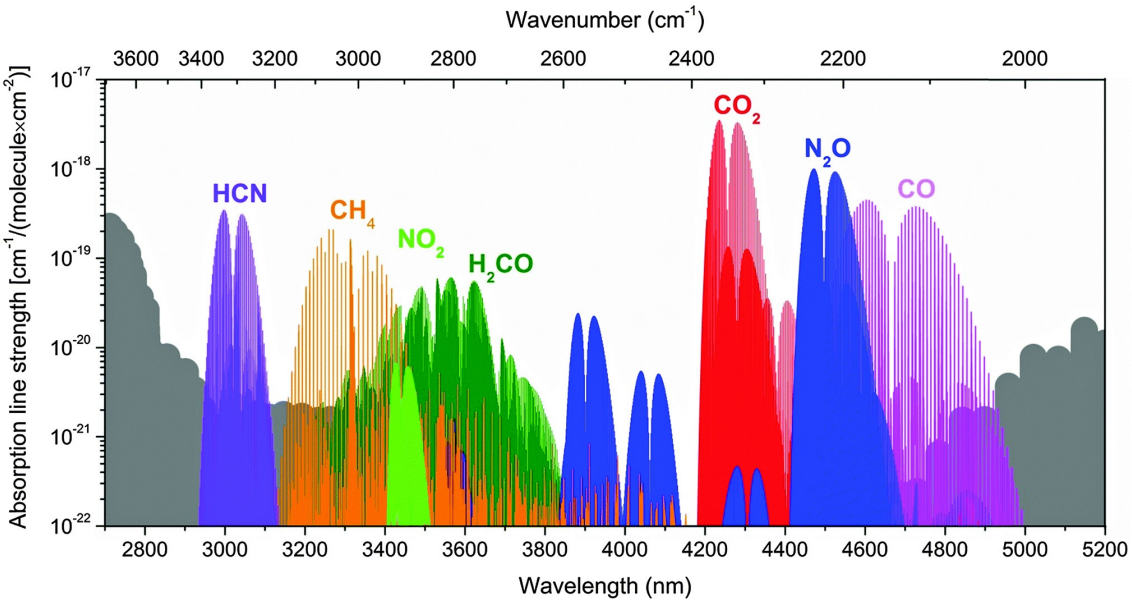

Figure 1.5: This graphic denotes various vibrational absorption spectra bands of compounds (grey area denotes water absorption band) [4].

Another application for SCG is spectroscopy and detection of hazardous compounds. Many chemical compounds have fundamental vibrational bands within the MWIR region [see Figure 1.5]. The advantage of SCG fiber devices is the compact, robustness that they would exhibit when used in commercial environments. The atmospheric transparency bands shown in Figure 1.1 allows for detection of climate changes, fossil fuel sensing, and pollution gas monitoring possible. Detection of carbon dioxide (CO_2) and monitoring of safe emission levels is extremely vital for safety. These emission levels can be very dangerous around heavy manufacturing environments, power plants, and high traffic areas. CO_2 is also a deadly gas when not controlled and monitored properly. CO_2 contributes $\frac{3}{4}$ of greenhouse gas emissions world-wide and has negative effects on the environment and our health. Absorption

bands for this gas and several others [see Figure 1.5] lie in the MWIR band easily covered by MWIR SCG lasers.

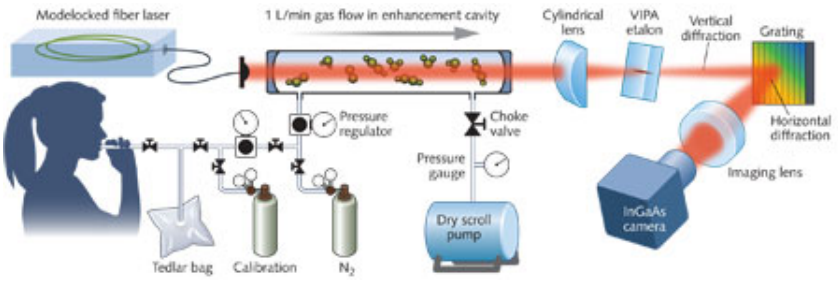

Figure 1.6: Example of a breath analysis system. This system uses a mode-locked laser to detect specific volatile organic compounds but broader bandwidth sources have the ability to scan a larger number of breath biomarkers [5].

Another application utilizing fundamental absorption bands of chemical compounds is related to medical sensing technologies. Extensive research has been conducted on non-invasive methods of monitoring certain diseases. Many of these devices can operate by simply using breath sensing to detect components in the ppm or ppb range [Figure 1.6]. In 1971 it was discovered that there are hundreds of volatile organic compounds (VOC) contained within human breath [15]. 35 biomarkers have been established within human breath and among those, 14 have been been analyzed using laser spectroscopy [16]. Certain VOC have been proven as indicators of specific diseases or metabolic states. For example, individuals with Type 1 diabetes have an excess concentration of acetone in their breath. Also, specific combinations of VOC can be biomarkers for diseases. An example of this would be the determination of schizophrenia from the presence of carbon disulphide and pentane [17].

1.2 Tellurite Glasses

Tellurite is the common name for the compound tellurium dioxide (TeO_2). Tellurite is the most stable form of TeO_2 and is most commonly used as a MWIR transparent glass. The most desirable traits for tellurite are low phonon energy, high refractive index, and also a nonlinearity that exceeds a value thirty times that of silica [18].

Tellurite glasses were reported first by Brady in 1956 when he showed the ability of TeO_2 to form a glass matrix by fusing a minimal amount of lithium oxide (Li_2O) into the melt [19]. A year later, Winter discovered the ability of tellurium along with the other Group VIa elements are known to produce monoatomic glass [20]. Monoatomic, or primary glass, is a structure that can be produced by one type of atom. Although tellurium could produce a monoatomic glass, increased stability was achieved when creating a binary glass by introducing a modifier (M) to help toward glass formation. Brady discovered as early as 1957 that a modifier was necessary in concentrations greater than 10 mol% before seeing any tendency to form a stable glass structure. In 1978, Mochida et. al delved deeper into the formation of many

Table 1.1: Glass-Forming Ranges of Binary Oxide Tellurite Glasses [21]

Second Component	**Lower Limit mol%**	**Upper Limit mol%**
$LiO_{1/2}$	20.0	46.3
$NaO_{1/2}$	10.0	46.3
$KO_{1/2}$	2.5	34.6
MgO	10.1	40.4
BaO	2.5	35.8
ZnO	2.5	45.0

different compositions of several binary tellurite compositions. He looked into both $MO_{1/2}$-TeO_2 (M = Li, Na, K, Rb, Cs, Ag, or Ti) and MO-TeO_2 (M = Be, Mg, Ca, Sr, Ba, Zn, Cd, Pb) glasses [21]. The glass forming ranges for several binary tellurite compositions can be seen in Table 1.1.

TeO_2-Zinc Oxide (ZnO) glass system are known to be one of the most stable and chemically resistant tellurite binary compositions. Adding Zinc Chloride ($ZnCl_2$) in place of ZnO is known to provide a dehydrating effect to the glass but it does not come without drawbacks. The addition of $ZnCl_2$ in place of ZnO can cause the glass to decrease in surface tension and therefore stiffness of the material. Glasses with $ZnCl_2$ as a modifier also have a greater tendency to exhibit crystallization when drawn down to fiber. A report of glass composition studies using ZnO and $ZnCl_2$ within tellurite glass system can be seen within Zhou et. al [22]. ZnO glasses are considerably more favorable for draw stability over their halide counterparts.

Tellurite is also known for its resistance to chemical attack. Tellurite glass is resilient to water, alkali and acids [23]. Water durability, or the hydrophobic capability, of a glass is shown in the susceptibility of the glass to resist weight deformation. Stanworth has shown that by introducing zinc within a tellurite glass system the material demonstrated no increase in weight with exposure to water over a several month period. He also conducted experiments to test the effect of acids and alkalis on a binary barium tellurite glass. The results showed that these glasses resist acidic attack but are known to be affected significantly by alkali [23].

Barium oxide (BaO) is a common additive for many tellurite glasses and has been investigated extensively as a binary modifier in tellurite glass systems [24]. This compound can be used to help generate a greater amount of Raman bands within the glass [25]. The fact that tellurite exhibits substantial Raman effects makes it very attractive for several nonlinear applications [26]. Tellurite fibers have exhibited

a Raman gain coefficient of 22.6 x 10^{-11} cm/W at 1.55 μm which is 35 times higher than silica glass [27]. The high nonlinearity within tellurite fibers makes it easy to be used as a gain-flattened Raman amplifier requiring much smaller pump powers than silica fibers to achieve similar effects [18, 25, 26, 28–34].

	Silica (SiO_2 based)	**Tellurite (TeO_2 based)**	**Fluoride (ZrF_4 or AlF_3 based)**	**Chalcogenide (chalcogen S, Se, Te based)**
Refractive index n at 1.55 µm	1.46	2–2.2	1.5–1.6	2.3–3
Nonlinear refractive index n_2 ($\times 10^{-20}$ m^2/W)	2.5	20–50	2–3	100–1000
λ_0, zero dispersion wavelength of material (µm)	~1.3	~2	~1.7	>5
IR longwave transmission limit	up to 3 µm	6–7 µm	7–8 µm	12–16 µm
Thermal stability for fiber drawing	excellent	good	poor	good
Viscosity around fiber drawing temperature	flat	steep	steep	flat
Durability in environment	excellent	good	poor, hygroscopic	good
Toxicity	safe	safe	relatively high	relatively high

Figure 1.7: Comparison of optical, chemical, and physical properties between silica, tellurite, fluoride, and chalcogenide glasses [27].

Tellurite is one of the few MWIR transparent glasses that is stable and can be drawn down to fiber with minimal effort. Other MWIR transparent fibers include chalcogenides and fluorides. MWIR fibers fabricated from heavy metal fluorides and chalcogenides typically have poor physical strength and can degrade over time. These significant reliability issues have been a major barrier in using these fibers for practical applications [35]. Recent reports have shown tellurite fiber strength extending to 60 kpsi [12]. Also, heavy metal fluorides exhibit low nonlinearity [36] and an aversion to water, unlike tellurite. Chalcogenides have much higher nonlinearity than tellurite but many of these glasses have a zero dispersion wavelength substantially far away from 2 μm, distancing themselves from available pump schemes [3].

Soft glasses differ significantly from silica glasses, which can be produced using

the modified chemical vapor deoposition process. Tellurites and other soft glasses require melt casting within a crucible. To produce tellurite glass that can be fiberized, extremely pure (>99.999% purity) TeO_2 is used along with several other ultra-high purity glass formers. Common glass formers for tellurite may include, but are not limited to: Li_2O, Na_2O, K_2O, ZnO, and BaO. Our glass that we received for this research project was melt at Kigre Incorporated, based out of Hilton Head, South Carolina which specializes in producing high quality laser glass.

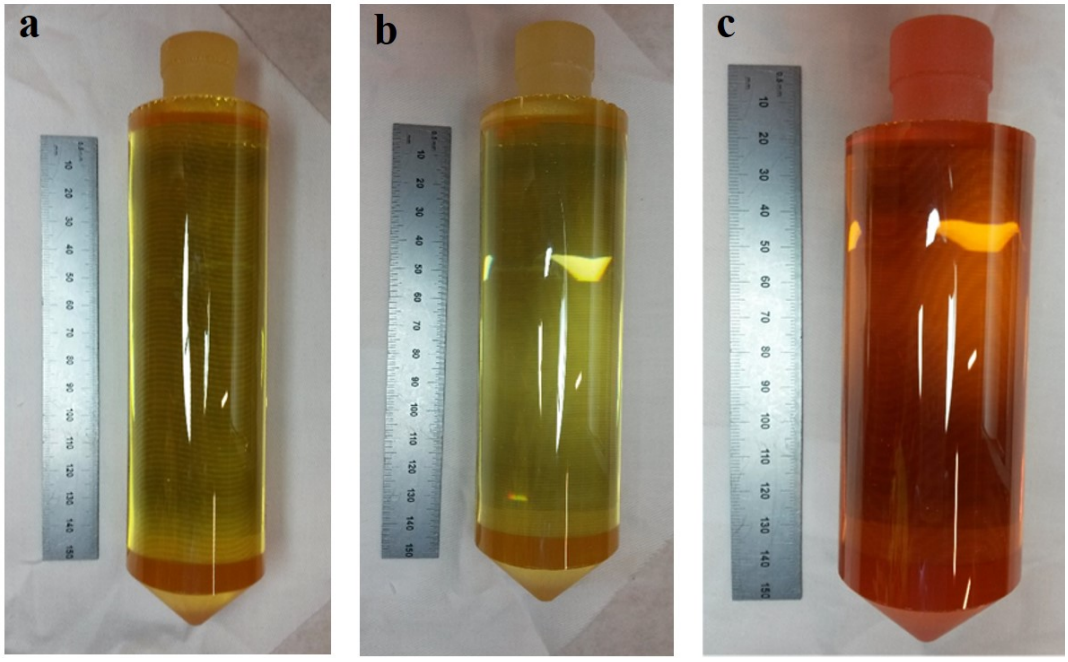

Figure 1.8: Tellurite preforms received from Kigre: a) Base tellurite glass; b) La-doped tellurite glass; c) Er-doped tellurite glass.

Kigre compositions and processes for tellurite high quality laser glass are described in a paper by Zhou et al. [22]. This work studies the effect of various modifier concentrations and the methods of reducing crystallization effects. Within this paper, Kigre produced multiple compositions of tellurite glass but focused on those with the base composition of tellurium-zinc-barium. Each of the preforms that we received

were optimized for glass stability and increased transmission within the MWIR band. Glass stability is an issue that requires careful consideration because during the fiber draw process a strong resistance to devitrification is required. Fortunately, tellurite glass has a much greater draw ability compared to chalcogenides and fluorides. The tellurite we received was batched using raw solid components. The raw glass melt was prepared in a silica crucible. After the pre-melt process, the glass was poured in a platinum crucible to set properly. The glass is mixed several times within the platinum crucible to provide a homogeneous melt. After the glass is cooled down it is set within an annealing furnace. The glass is annealed within the glass transition temperature (T_g) and the softening point. The glass would be annealed slightly above 328.68°C. After this annealing process, the outer surface of the tellurite rod will have a rough finish. The next steps all would include producing a more aesthetic preform and designing any fiber draw support aids.

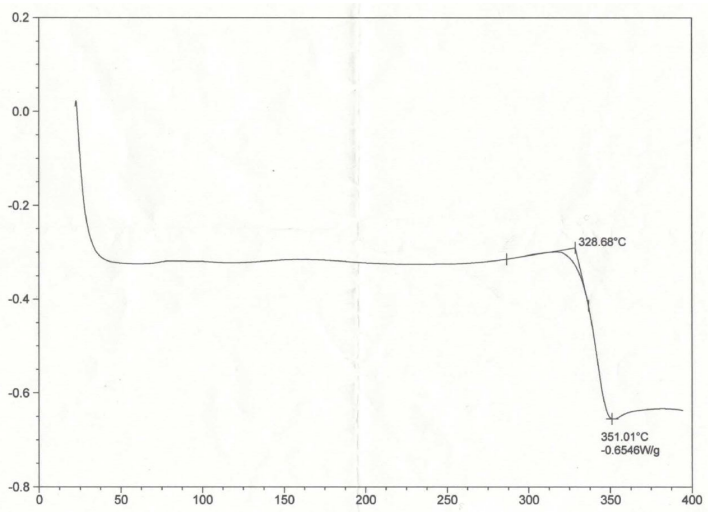

Figure 1.9: This DSC curve of the tellurite base glass was conducted at Kigre Inc. after the fabrication process. The y-axis is a representation of Heat Flow (W/g) while the x-axis demonstrates the Temperature (°C). The annealing temperature of a glass is determined by the sharp drop off in heat flow.

The knowledge employed in [22] was used to produce the tellurite glass pre-

forms that we received. The glass we received was optimized for low liquidus temperatures and extended spectral transmission in the MWIR band. The solid additions were TeO_2, BaO, and ZnO [see Table 1.2]. Kigre's glass composition paper went through 44 hand melt compositions before finally settling upon a composition that was optimized. The TeO8-23 hm composition was very similar to the base glass that we received. The differential scanning calorimetry (DSC) measurement can be seen in Figure 1.9. This glass shows no evidence of crystallization and has a T_g of 328.68°C. This glass transition temperature is very similar to other tellurite glasses with comparable binary compositions [37].

Table 1.2: Component Concentrations from EDX in mol%

Composition	**Concentration in mol%**					
	Te	O	Ba	Zn	Er	La
Base Glass	50.97	19.48	17.84	8.16	0.00	0.00
Er-doped	48.50	19.54	16.96	7.69	4.13	0.00
La-doped	45.12	19.61	19.68	5.29	0.00	7.84

Tellurite glass stands out from other MWIR transparent glasses for many physical characteristics that we have mentioned but the main reason it is utilized is the nonlinear properties that are ideal for the SCG experiment. Silica glass may be the best glass for telecommunications applications due to the zero dispersion wavelength (ZDW) being located at 1.3 μm and the loss being among the lowest demonstrated in any optical fiber, but the transmission window does not extend into the MWIR region and therefore cannot be used for several of the defense and sensing applications that we desire. Also, tellurite glass exhibits a nonlinear index that is an order of magnitude higher than silica and fluoride glasses. This leaves chalcogenides and tellurite as the two standout glasses for supercontinuum generation. The property that proves

tellurite is a more attractive solution would be the ZDW that is within range of available pump schemes. Chalcogenides have a ZDW that ranges from 5 – 10 μm and is too far away from a reliable mode locked laser source that can provide high power. Tellurite's ZDW lies right at the 2 μm region which is conveniently placed at the Thulium (Tm)-doped mode locked lasers pumping wavelength. Tm-doped fibers are located close to the MWIR wavelengths and can be produced robustly with mature silica fiber technology. Tm-doped mode locked lasers are an advanced technology that has been shown to scale in peak power and can be easily pulsed with minimal effort. Recently, kW-level continuous wave Tm-doped fiber lasers have been demonstrated due to the efficient 2-for-1 process which enables the use of high-power diodes at 795 nm as pumps [38]. Tm-doped fiber lasers can therefore provide a path for potential average power scaling to hundreds of watts for MWIR sources.

Chapter 2

Optical Fiber Drawing

Fiber has been used as a communication medium for over a century. It wasn't until the 1980s though that optical fiber made a huge leap forward to be used for telecommunications, replacing copper wire in long haul situations [39]. The first glass spun fiber was fabricated by Rene de Reaumur in 1713 but was not used for communication purposes. The next advancement was the invention of the optical telegraph by another French scientist, Claude Chappe, in 1790. The optical telegraph was a major improvement in optical communications, but would shortly be replaced by the electrical telegraph. At this point in history, optical technology was nowhere near the maturation that electrical communication had reached. Also, the system required open atmosphere and could not provide the security and implementation ease that the electrical telegraph allowed. For nearly two centuries, electrical signals carried by copper wire were the technology of choice.

The first discovery of light guidance or total internal reflection (TIR) through a medium was not in glass but rather a stream of water [see Figure 2.1]. Just a year later, a different researcher also discovered TIR through not only water but bent glass rods as well. In 1880 the photophone was invented by Alexander Graham

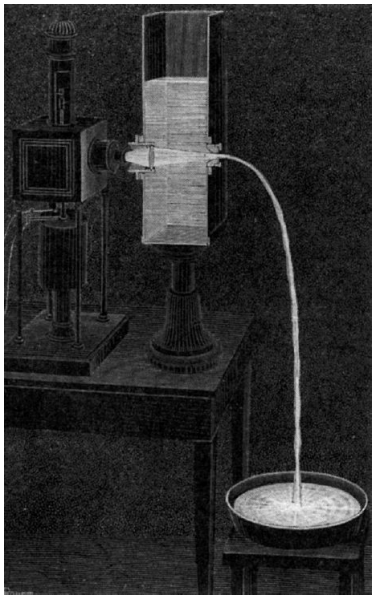

Figure 2.1: First crude demonstration of total internal reflection within a stream of water [39].

Bell. The photophone was so revolutionary because it was the first instance of speech transmission through light. The photophone was unsuccessful though due to issues with the equipment required to keep it sustainable and was eventually overtaken by the telephone. In 1898 a patent was filed by David D. Smith for the use of bent glass rods to be used as a surgical lamp. Throughout the beginning of the next century, various methods of light transmission through glass fibers were produced. Many of these developments involved crude imaging through the use of bundled glass optical fiber. The first glass clad optical fiber was produced in 1956 by using the rod in tube fabrication method to produce a higher index core [see Figure 2.2].

In 1958, Schawlow and Townes developed the theory behind the operation of a laser and this breakthrough opened up the floodgates for several important discoveries in years to come [41]. In 1959 Elias Snitzer developed a theoretical description of single-mode (SM) waveguides [42]. Less than a year later, a fiber was drawn down so finely that various modes were observed within the fiber [43]. In 1960 Theodore

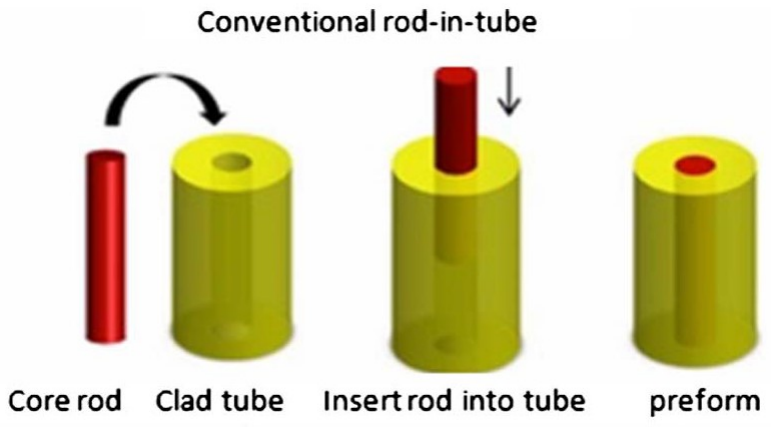

Figure 2.2: Depiction of the rod-in-tube preform fabrication method [40].

Maiman created the first laser, utilizing a ruby gain medium [44]. In 1966 Kao made the groundbreaking claim that 20 decibels/kilometer (dB/km) fiber loss, suitable for telecommunications, was feasible [45]. Within the next decade, several other discoveries led to lower loss fiber and more efficient diode lasers. In 1976 however, the first extremely low loss fiber was fabricated in Japan at NTT Ibaraki Lab and had a loss of 0.47 dB/km at 1.2 μm. Two years later, the same lab produced 0.2 dB/km at 1.55 μm [46]. In 1987 the modern telecommunications industry began with the invention of the Erbium-doped fiber optic amplifier [47]. In 1989 the first transatlantic fiber optic cable was laid [39]. After these recent discoveries, the telecommunications industry has grown at exponential rates. Within the last 25 years new technologies and approaches in the fiber optic community have been implemented for medical, defense, sensing, and large-scale production applications. Fiber optics have revolutionized our daily life and it only takes a moment to realize where you have been affected.

As I mentioned previously, the first developments with light guides were water streams, but the next big leap in optical fiber was the invention of a metallic waveguide in the 1930s. Although these fibers reported a loss of 2 dB/km they were far too expensive to produce and demonstrated too narrow of a bandwidth limiting future

expansion in the area [39]. After the invention of the laser, research really expanded towards production of glass optical fibers, but not before looking at lens-trains and gas-filled pipes. In 1970 however, Corning was the first laboratory to develop a fiber with loss values lower than that which was proposed by Kao, <20 dB/km [48]. The fundamental requirements for producing optical fiber are the ability for the material to be produced in large quantities uniformly while also having a designated core and cladding index to provide TIR. This fiber must also be made from a purified material that permits the wavelength that you wish to use for communication. While this may sound relatively easy, it is difficult to meet these expectations for telecommunications grade fiber.

When you discuss glass in a general sense, you are often referring to quartz which is the natural crystalline form of silica. Quartz is the main component of sand and is mixed with sodium carbonate (soda) and calcium oxide (lime) to produce soda-lime silicates that are easier to fabricate than pure silica. Telecommunications grade optical fibers are produced from liquid raw materials with high vapor pressures. This process employs mixing silicon and oxygen at high temperatures to produce SiO_2 or silica glass. Silica is the most widely used material for optical fiber not only due to its strength but also the optical properties that this fiber presents. Mass production of silica optical fibers begins as an extremely pure tube or mandrel that goes through a vapor deposition process. Liquid components are used as the starting materials effectively producing a final product that is significantly purer than any batch melted composition. Producing glass from liquid components is cleaner due to the liquid ingredients having high vapor pressure. This process allows trace heavy metals that may be in the liquid solution to remain trapped rather than be vaporized with the pure material. The chemicals are introduced into the preform by a gas delivery system. The mixture is deposited as a porous soot when introduced at high temperatures.

The preforms can also be further doped by introducing the dopants using a liquid solution into the porous soot. After the doped material is introduced, the entire preform is collapsed onto itself and then resembles an optically clear solid rod. This process is slightly altered depending if the preform was produced within a silica tube by modified chemical vapor deposition or was constructed on a mandrel by outside vapor deposition. Although this method cannot be surpassed, in terms of purity, for solid silica fiber many other fabrication methods need to be implemented for air-clad or air-core designs. Additionally, many soft glass preforms must be fabricated from a batch melt composition.

After the fabrication of a glass, the preform is ready to be drawn down to fiber. The process begins by chucking or holding the glass preform up above the furnace, which can be approximately 10 – 20 ft from ground level on a research draw tower. The draw tower used at Clemson University can be seen in Figure 2.3. The preform is lowered into the furnace so that the end of the glass is positioned approximately 10 mm below the hottest region of the furnace, or the hot zone. After the glass is positioned and the purge gases are raised inside the furnace to give an inert environment, the furnace is set to what is called the drop temperature (T_{drop}). The T_{drop} is when the glass in the hot zone begins to soften and cause the bottom region of the preform, termed the "drop", to fall due to gravity. The ideal drop viscosity is approximately 10^9 $g/cm^{-1}/s^{-1}$ or poise (P). After the drop falls, the large glass end is cut off and the thinner, fiber-like, section is pulled down the tower and through the capstan. The section where the glass begins to fall from is called the neck-down [see Figure 2.4]. The neck-down is the region where the preform reduces to the size of the final cane or fiber.

The outer diameter (OD) of the fiber is controlled by the ratio of the rate that the preform is fed into the furnace and the speed that the fiber is pulled along the

Figure 2.3: Clemson University draw tower with soft glass furnace in place.

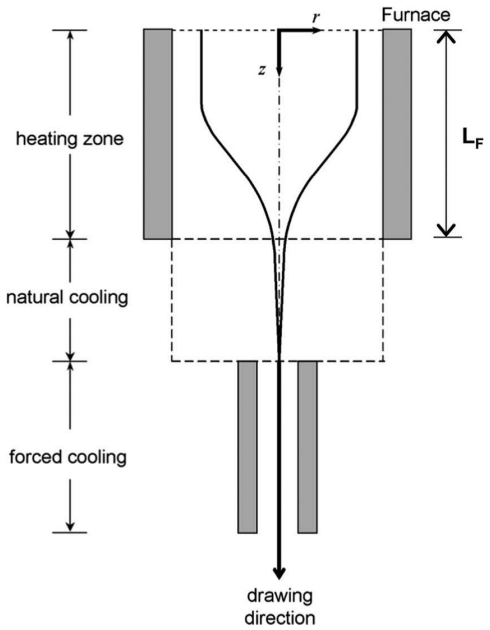

Figure 2.4: Depiction of the neck-down region in the furnace [49].

capstan. The equation for this process is listed in Equation 2.1.

$$D_{\text{fiber}}(\mu m) = (\frac{Feed(mm/s)}{Line(m/s)}) * D_{\text{preform}}(mm) \tag{2.1}$$

The OD of the fiber is continuously checked as the fiber is pulled through the two diameter monitors. The diameter monitors are located below the furnace and directly above the capstan. A fiber's ideal draw viscosity is approximately 10^6 P to allow for tension so the fiber remains taut but also the flexibility to be pulled. After the fiber is at the correct diameter and running stable, then the fiber is clad with a coating for protection. The coating is typically an acrylic that is cured using an ultraviolet curing unit. After the fiber is coated and the OD of the outer layer is checked using the bottom diameter monitor then the fiber can be taken from the capstan and placed on the drum winder which lays the fiber on the spool. After this process is complete, the spool will continue to move sideways so that the fiber will be laid down concentrically

without overlap. Different draw processes may be implemented if an experimental composition is used or special coating required.

2.1 Stack and Draw Method

The stack and draw method is a relatively new process of producing specialty fiber designs, namely the photonic crystal fiber (PCF). This fabrication process was created by J.C. Knight et al. in 1996 [50]. This process allows one to create a macroscopic geometry that then translates to a similar desired microscopic geometry. Fibers with an air cladding were traditionally made by using preform drilling. The stack and draw process was determined to be a simpler and more controllable way of creating a fiber design with air hole cladding.

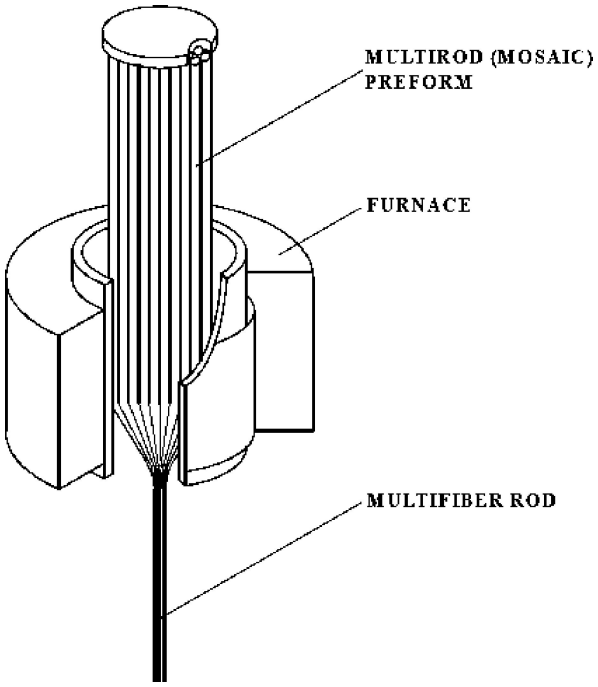

Figure 2.5: Stack-and-draw preform shown within furnace drawing down to cane [51].

The stack and draw method begins by first planning and simulating the pro-

posed design. After a microscopic structure has been determined and tested, then the macroscopic design can be fabricated [see Figure 2.6]. If the preform requires an air core structure then capillaries need to be drawn down to a small size to be handled easily and fit within the proposed stack design. Typically all of the constituent materials of a stack are the same general glass composition and require each component to be the same size. We chose canes and capillaries to be 1.5 mm in OD for all of our stack designs. This size of cane is easy to handle and can provide the rigidity and support that each stack needs to complete macroscopic structures. Our stack sizes ranged from 7.5 mm to 43.5 mm in OD. The size of the stacks were determined by the core to cladding ratio that we wanted to achieve and if the design required a two stage process. This fabrication process is easy to use and can provide a simple solution to some rather complex fiber designs.

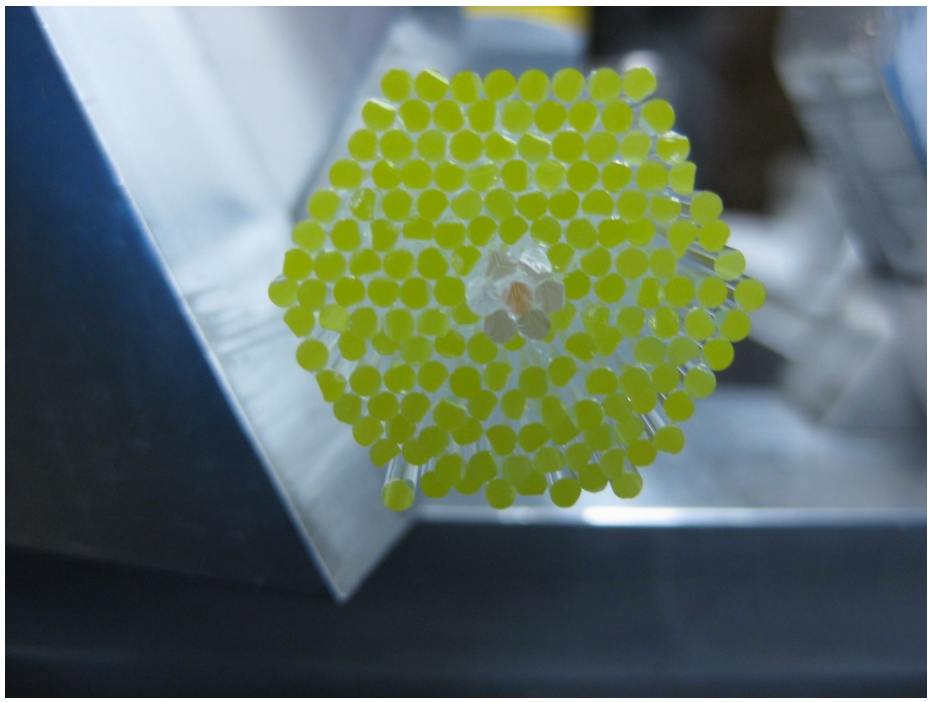

Figure 2.6: Macroscopic preform stack showing the hexagonal arrangement. This stack represents at tellurite core and phosphate cladding.

Air cladding or air core designs prior to the stack-and-draw's discovery were conceived by core drilling of the preform material or by performing an extrusion process for soft glass materials. While this process can make incredible structures otherwise unobtainable, they require highly specialized equipment. These alternative processes also requires completely inert materials. If the die and drilling materials are not controlled properly the perform may be contaminated with heavy metals that can degrade the glass [52].

After the preform design has been simulated and confirmed then the process of arranging the canes and capillaries begins. To provide the correct template a stock hexagonal guide rod is set into the stacking clamps to confirm size. After this is complete, the guides are set and stacking may begin. Adjustability between preform sizes is easy to implement. One of our first stack designs [see Figure 2.6] and our finalized stack design [see Figure 2.12] have an area difference of nine times. This method requires no specialized equipment and can produce a broad range of designs.

Each rod is cleaned with ethanol carefully. After wiping down the rod with ethanol, the glass is run through a deionizing air knife. Once the rod is confirmed clean then it is laid within the hexagonal guides set for the desired design [see Figure 2.7]. This stacking process continues for several rows alternating doped rods or capillaries depending on the preform design. Once this process is finished, the preform then undergoes a tacking step to secure the material. Finally, depending on the preform the glass will be sleeved inside an over-clad tube to pull everything together with vacuum. Occasionally pressure connections are added with holey structures to ensure proper capillary opening occurs.

We wanted to utilize a stack-and-draw process with the tellurite glass due to the set-up simplicity and repeatability. The stack-and-draw fabrication method does not require any expensive equipment and can be implemented with ease. With solid-

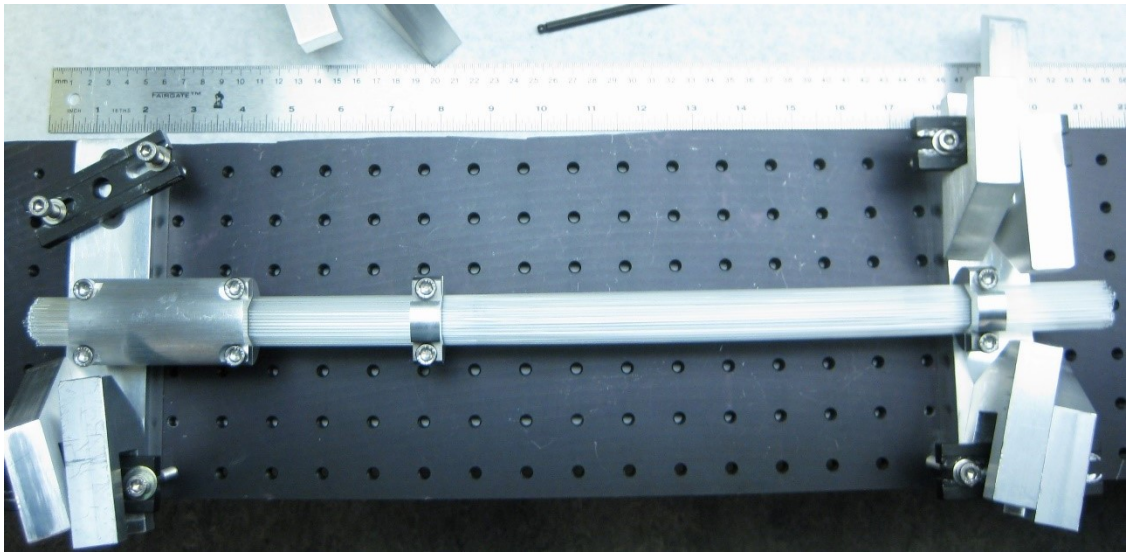

Figure 2.7: Large preform constructed using the stack-and-draw method with aluminum hexagonal clamps.

core soft glass structures, it also offers a simple way to create a desired fiber numerical aperture without the use of tubes. Here at Clemson University, we have developed the stack-and-draw method to be an effective fabrication method for PCFs, photonic band-gap fibers , and leaky channel fibers. Utilizing this mature fabrication method for creating a solid-core tellurite fiber for SCG has not been implemented before.

2.2 Tellurite Glass Fiber Drawing

Tellurite glass was first recognized as a great optical fiber candidate in 1994 [53]. Tellurite has incredible draw stability for a soft glass optical fiber and demonstrates excellent robustness. Strength of a fiber is an important quality so that real world events will not disturb operation. Also, the draw ability of the optical fiber is extremely important. Draw ability can relate to properties such as thermal stability, crystallization potential, and toxicity. Further knowledge of your specific glass composition can help significantly when performing the fiber draw step.

Determining the draw properties of the material that you are producing improves your capability to predict the behavior of glass may have when being fiberized. Several thermal effects such as DSC can be implemented beforehand to understand the temperatures required to draw your glass. The material we received has much larger surface tension than chalcogenide and fluoride glasses but much smaller than silica. This property allows the glass to maintain the shape of the current design without much deformation. The material also has a large thermal expansion coefficient (α_{th}) difference compared to fused silica, almost by a factor of two. The thermal expansion coefficient difference of silica α_{th} is approximately $0.55\text{x}10^{-6}$ $^{\circ}\text{C}^{-1}$. This is significantly lower than the values discovered by Stanworth in 1952 for tellurites. His discovery showed a α_{th} for a tellurite-barium-zinc composition of $20\text{x}10^{-6}$ $^{\circ}\text{C}^{-1}$. This large thermal expansion value makes melting tellurite with other materials extremely tricky. We attempted drawing several solid tellurite fibers with other soft glass material cladding but encounter significant interface issues. The only cladding materials that proved successful, through drawing and cleaving steps, were tellurite glasses with a similar α_{th}.

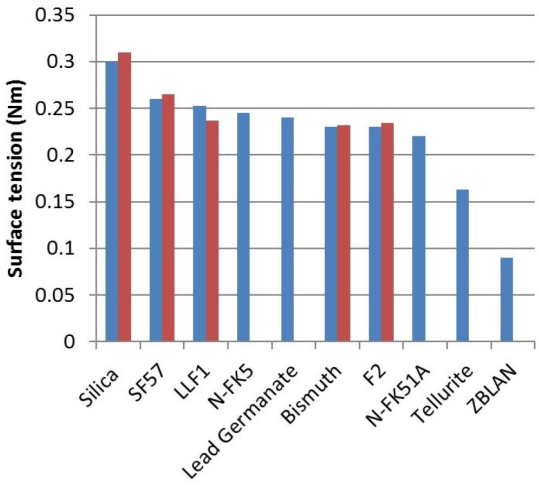

Figure 2.8: Surface tension values between commercial silica glasses and various soft glasses [54].

Tellurite is also known for having a very small viscosity range for fiber drawing [55]. We explored the idea of using phosphate glass as cladding because it had similar α_{th} values and provided a relatively close optimal draw temperature. Even using substantial layers of cladding and drawing at the low end of the phosphate draw range, we were unable to keep a uniform core structure and therefore had to move to using an all tellurite structure. The glass forming range for tellurite is only within 50°C which is significantly lower than silica glass. During our fiber drawing process, we noticed that we only had a range of 5°C that allowed us to produce a fiber with the desired core and clad structure.

2.2.1 Glass Rod Fabrication

The fabrication of the tellurite capillaries or canes from a preform is the first step to producing a stack-and-draw structure. We received the three preforms: a base glass tellurite, Er-doped tellurite, and La-doped tellurite [see Figure 1.8]. Each preform had a ground down nub on the top end of the preform per the design located in Appendix B Figure B.2. Due to the large distance we have from the glass chucks and the top of the furnace we required a method of gripping the preform and extending our length via a handle. This nub allowed us to grip the preform with a stainless steel clamp and permitted us to draw the entire preform by extending our length with a stainless steel rod. The bottom of the preform was machined down to a tip because the furnace exit was too small for the entire preform to come through with the drop. This tip allowed us to get a small drop from the preform and use less of the preform for startup so more canes were allowed to be drawn.

We purchased the three glasses with the intent to try two different preform designs. Refractive index matching with Erbium (Er) and Lanthanum (La) as dopant

materials has also been shown and proven to work well [56]. The first design would be a passive tellurite fiber with base glass core and a La-doped tellurite cladding. Our second design involved a Er-doped tellurite fiber for emission at 2.94 μm. This fiber would have an Er-doped tellurite core and La-doped tellurite cladding. Er^{3+} has an emission at 2.94 μm that is extremely useful for several applications. We were intending for this preform to be used in medical applications very similar to Urich et. al [57]. This emission is extremely desirable due to the OH absorption band at this wavelength.

To choose our preform draw order, we decided to perform the Er-doped tellurite glass draw first because we needed a small amount of canes for the draw and learning the temperature profile would take some time. Next, we would draw the base glass tellurite preform because we did not need much of this glass for our passive core designs. Lastly, we drew the La-doped tellurite cladding because this preform required canes to be implemented into both active and passive designs that we desired. By drawing this glass last we would have a better understanding of the temperature profiles and how the glass should behave. We prepared all preforms for the draw by simply wiping them down with ethanol on a lint-free wipe and blowing them clean with nitrogen before chucking them into the furnace. The draw temperatures and amount of canes or cappillaries collected for each preform drawn down to 1.5 mm OD can be seen within Table 2.1.

The Er-doped preform was prepared for drawing first. We were successful drawing this preform at 475°C. Due to the fact that this was the first preform we did draw, we were quite slow in increasing to the T_{drop} and afterwards lowering to the correct draw temperature (T_{draw}). The T_{draw} is a very critical setpoint and required much tweaking to get correct. The surface finish of the preform looked exceptional and the diameter tolerance was quite narrow. We were able to draw approximately

60 - 1 m lengths of 1.5 mm OD cane.

Table 2.1: Comparisons Between Different Preforms

Properties	**Preforms Drawn to Cane/Capillaries**				
	TeO_2 Tube	TeO_2 Rod	Er-doped	La-doped	Phosphate
Rare Earth wt%	0	0	2	5	0
Draw Temp (°C)	445	445	475	520	670
Drop Temp (°C)	490	500	520	550	730
Quantity of Canes	100	75	60	10	100

After fabricating the Er-doped preform we moved to the base glass preform. This preform did not have the extra dopants added to the melt and therefore we suspected it to draw at a slightly lower temperature. This glass drew at a temperature of 445°C. The surface quality of this preform was very clean and due to our familiarity with the draw temperature and behavior of the glass we were able to draw more canes. We successfully drew approximately 75 - 1 m lengths of 1.5 mm OD cane with little variation in size.

Finally, we drew the La-doped tellurite preform. This preform needed to provide greatest number of canes in total for both stack designs to work. We required a large number of La-doped canes because the glass has a depressed RI compared to both the base glass and Er-doped glass and it was to be the cladding glass for both preform designs. While erbium and lanthanum typically cause a refractive index increase when added to silica glasses, it lowers the index when introduced to a tellurite structure. This is due to the fact that tellurium has a much higher atomic weight compared to silicon. Lanthanum also has no active regions in the MWIR band that would cause an issue with Er-lasing or MWIR SCG. Due to these reasons, it makes an excellent passive glass additive within the tellurite glass structure.

The La-doped tellurite preform was drawn in the same manner that the canes from the previous two tellurite preforms were produced. The preform was lowered into the furnace and was raised to the T_{drop}. We predicted the preform to have a much greater T_{drop} than the base glass and thought it would be comparable to the Er-doped tellurite. Although the former was true, the La-doped glass had a significantly higher drop temperature, nearly 50 °C greater than even the Er-doped tellurite.

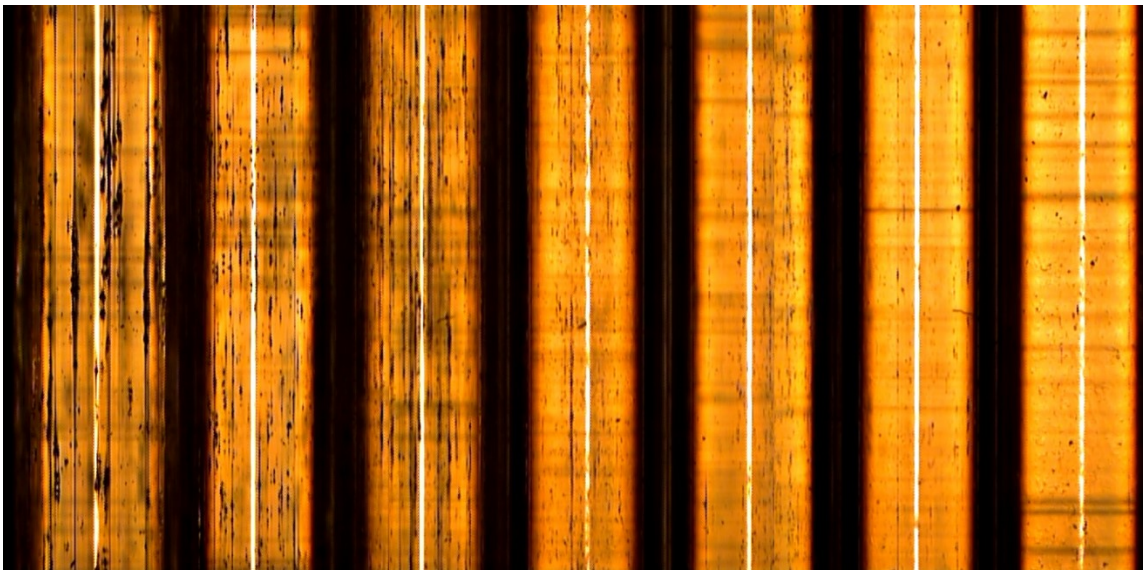

Figure 2.9: Shown is the lanthanum canes transition through draw. The canes crystallization decreased as the draw progressed (moving from left to right). This was largely due to the faster speed and higher temperature of the furnace.

The La-doped tellurite glass began to crystallize during the drawing process. This was very clear from the beginning of the draw due to the rough surface and weakness of the glass. The La-doped tellurite glass was produced with a much higher dopant concentration than the Er-doped tellurite [see Table 2.1]. Due to this increase in RE concentration, we believe it caused instability in the glass when heated and the lanthanum started to come out of the stable glass matrix. As the draw progressed we had to develop a solution. The draw speed was increased along with the temperature to allow a lower amount of dwell time in the furnace. As you can see in Figure 2.9

the canes appeared to show significantly less crystal formation from the beginning to end of the draw (left to right respectively). By introducing the glass to a higher temperature and less dwell time in the furnace, the crystals have less time to form due to rapid cooling upon exiting the furnace.

The quantity of La-doped canes we collected was significantly less than both of the other tellurite glass compositions. We were able to collect approximately 10 - 1m length 1.5 mm OD canes that look similar to the furthest right cane pictured in Figure 2.9. Although we were happy to gather some canes, we later found out during the stacking process that these canes would be unusable for stacking designs. Although the stack-and-draw process can produce very clean final preforms, the interfaces were an issue. This is due to the increased surface area introduced with the fabrication process. Even the limited amount of crystals can cause strength issues. During the fiberization procedure, this created a very weak fiber.

A tellurite tube was produced from the outside layer of the base glass tellurite melt. We were able to receive from Kigre a tellurite tube and rod from a single batch melt. This was done by core-drilling of the rod. The tellurite rod we drew was then machined and polished from the center piece. Although this process allowed us to get two separate preforms, the tube had a rough exterior and we were unable to receive the smooth surface finish that the tellurite rod has. Figure 2.10 demonstrates the quality of the preform. This tube can be used for drawing capillaries but the inability to perform glass-working and difficulty in creating a longer tube make it impossible to be used as an over-clad tube.

After the tube was received we needed to develop a method of holding the preform. With a silica glass lathe, we could just attach this tube to another handle tube by using a glass-worked join. If two tellurite tubes were joined on a glass-working lathe, upon cool-down, they would crack at the join. We required the ability

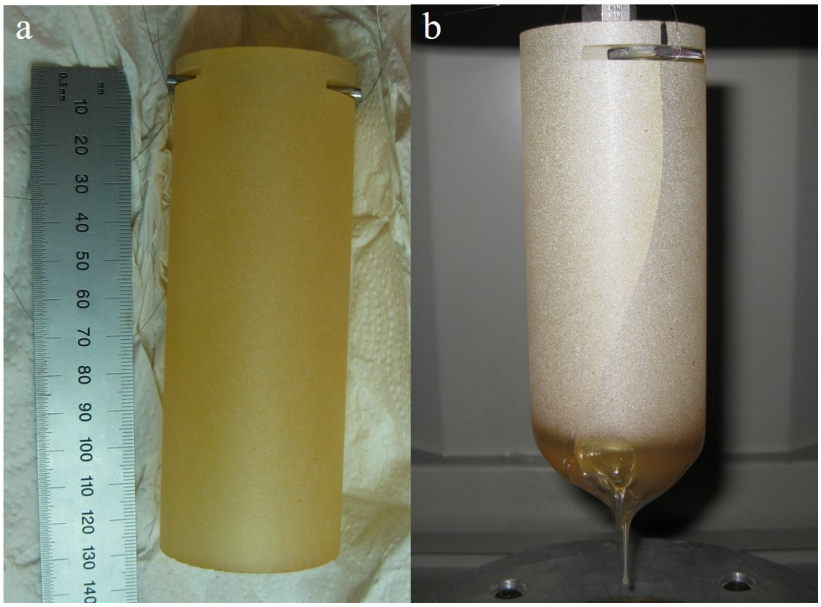

Figure 2.10: Tellurite tube depicting the metal shim used. Also on the right is the crack that was created after heating and forming a small neckdown.

to insert the entire tube into the furnace while using as much preform as possible. The extension process allows us to lengthen the preform so that we may use the entire section of research glass without worrying about distance from chuck to hot zone. We decided upon fabricating a holder support piece that would be inserted through the tube. We were able to achieve this by cutting a notch on both sides at the top of tube with a diamond tip saw. Next we inserted a thin stainless steel shim through the cut notches of the preform. This shim had a threaded insert in the middle which would attach to our extension rod. Finally we tightened stainless steel wire to holes on each side of the preform and used the thin wires to secure the preform to the middle.

Once the preform and metal shim were securely together, we threaded the hanger rod into the metal shim and tightened the wires to the rod. Although this setup is rather crude, it allowed us to keep the preform secure during the draw. The diameter of the preform was rather large so we first needed to pinch together the bottom piece of the tube so a small drop could fit through the throat of the furnace.

The draw was shut down to address some issues with start-up. Upon cooling of the preform, we were unable to anneal the preform properly. This issue created a large crack through the preform and the outside of the tube surface became even rougher [see Figure 2.10]. We attempted to draw the tellurite tubes the next day and the crack sealed. Upon reheating the surface finish cleaned up and we drew approximately 100 - 1 m lengths of 1.5 mm OD tellurite tubes. The neck-down at the end of the draw can be seen in Figure 2.11. The large gap is from the notched cuts in the tube stretching during the last stage of drawing.

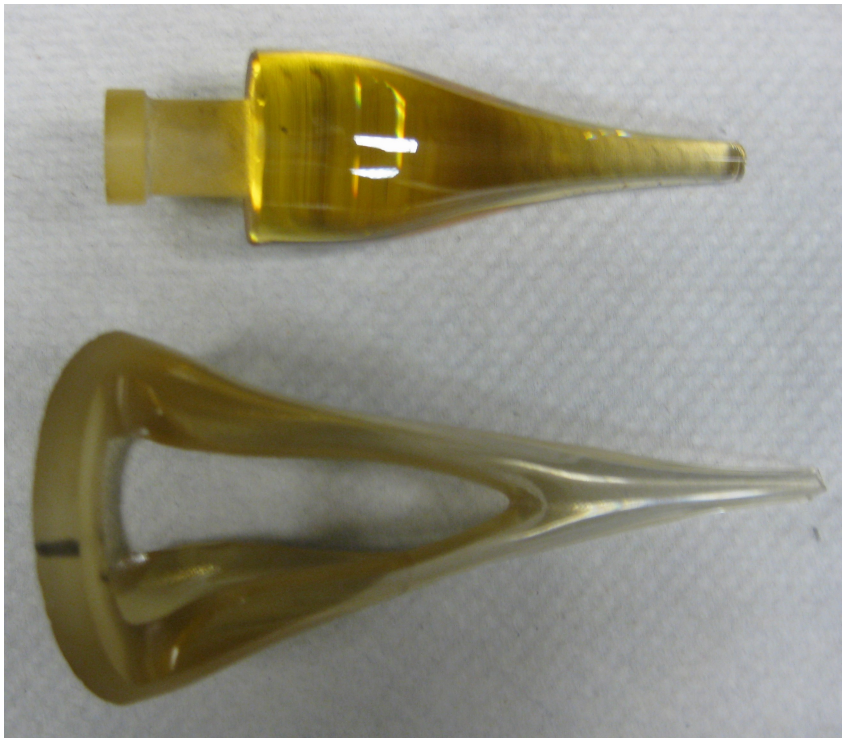

Figure 2.11: Neckdowns of the tellurite tube and rod.

This method of producing tellurite tubes is rather crude and does not allow us to produce an over-clad tube. The process of creating a soft glass tube is typically from core drilling or centrifugal rotation inside a silica tube [52]. While we do have a lathe in house, we had no method of creating tellurite tubes with consistency. The

main limiting factor was our limitation in an annealing oven. An annealing oven would mitigate the thermal stresses caused from heating and cooling down and allow us to safely produce a tellurite tube. Due to this issue, we developed a method of producing a tellurite stack without the use of an over-clad tube.

We also purchased several phosphate glass preforms to draw down to cane. The phosphate glass was to be used as a cladding option to provide us an inexpensive method to produce several fiber designs. We purchased a glass that would have a similar thermal expansion coefficient to tellurite glass. This feature is very important to reduce any chance of causing thermal stress issues during fiberization. We searched for the glass that had a similar α_{th}. We also needed the lowest temperature phosphate glass commercially available. The glass we purchased was L-TIM28 produced by Ohara Incorporated. L-TIM28 has a viscosity of 10^{-6} P at a temperature of 625°C.

The small preform was gripped by using a combination of a stainless steel tube fittings and teflon ferrules. Teflon has a lower melting temperature than the phosphate glass but withstood temperatures when outside the hot zone. Teflon also provided a strong yet flexible cushion for us to utilize it as a clamping force. After chucking the preform we drew down the phosphate glass and were able to receive approximately 100 - 1 m canes at 1.5 mm OD. We hoped that although this draw temperature was much higher than the tellurite glass, it would provide a cheaper alternative to an all tellurite stack.

2.2.2 Stack-and-Draw Process

The stack-and-draw process began by planning the desired preform design. The first preform we attempted was a tellurite base glass core with a phosphate cladding in the interest of saving glass. We decided upon a final fiber design that

would be a $\frac{1}{25}$ ratio between the core and cladding diameter. We achieved this design by using a two step process. The first step involves creating a stack that has a $\frac{1}{5}$ core to clad ratio. After this macroscopic design is drawn down to 7.5 mm corner to corner (C-C) cane then it is subsequently stacked into the same design with an outer clad of phosphate glass. The macroscopic design can be seen in Figure 2.6. The reason for the odd color in the core area is because we used phosphate glass also on the ends of the preform. By using just tellurite in the middle section, we can use the ends for startup and holding the preform.

The preform was stacked to create a design with a corner-to-corner dimension of 22.5 mm. The preform was stacked within the hexagonal guide templates and then was clamped together on one end. The end clamp was fabricated with a large hanging rod extending above it to allow the entire preform to be in the furnace regardless of length. While this holds the top end, the bottom end remains relatively loose. This issue was mitigated by clamping on the bottom end with another smaller hexagonal clamp and while tight, using thin stainless steel wire to wrap around the entire stack to keep the preform secure. The hexagonal clamp was then removed from the bottom end and the stack was finally secured on both ends and could be turned vertically for drawing. We have to go about using this method rather than traditional tacking to hold the glass together because of the high α_{th}. Due to this issue, if cooling can not be controlled properly the glass has a very high chance to crack upon cooling. While this process of using phosphate glass does reduce tellurite use and keep costs down, the viscosity difference between the two glasses at the same temperature was far to different to be used successfully. By raising the phosphate glass to a reasonable T_{draw}, the interior tellurite base glass would have an extremely high viscosity and would not remain uniform.

The next step was attempting to produce an all tellurite stack preform while

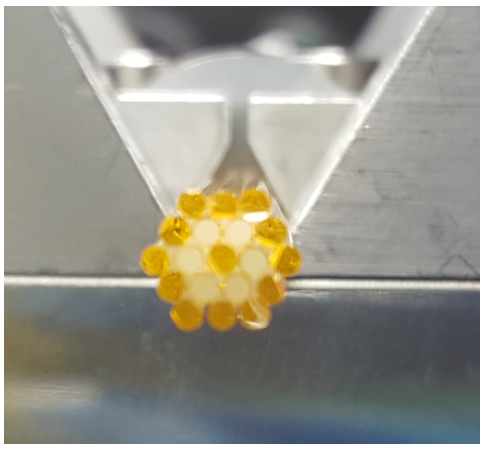

Figure 2.12: Cross-section denoting stack size of the all tellurite preforms. This stack shows an air-clad preform but the 7.5 mm C-C OD of the all tellurite stacks did not change.

also keeping material costs down. We were able to do this process by reducing the stack length from 800 mm to 200 mm. A more efficient way of reducing preform size was by cutting back the amount of canes we used. The new method allowed us to reduce the total number of canes used from 169 to 19, while using the same $\frac{1}{25}$ core to clad ratio. This was achieved by performing a two step stacking method, drawing down a first stack with 7.5 mm C-C OD to 1.5 mm C-C OD to provide the central cane for the second step.

Several stacks with a 7.5 mm OD and an all tellurite design were drawn. These tellurite stacks were drawn with Teflon^{TM} tape wrapped around the clamp/top end to secure a solid fit. The preforms were also held on the bottom end with stainless steel wire that fell along with the drop when the draw began. A 200 mm long stack was able to utilize approximately 140 mm of preform due to the top end being held inside the hexagonal extender clamp. An example of this clamp can be seen in Appendix B Figure B.3.

2.2.3 Tellurite Fiberization

The tellurite fiber fabrication begins shortly after the stack-and-draw process. The completed stack was then taken to the draw tower and the handle rod pictured in Appendix B Figure B.3 was chucked above the furnace. The preform was then lowered into the room temperature furnace. The bottom of the stack was placed approximately 10 mm below the hot zone of the furnace. After the preform is placed in the drop position, the N_2 purge of the furnace begins. The top and bottom iris of the furnace is adjusted to allow an inert atmosphere. After the atmosphere is controlled properly, then the furnace is raised to the drop temperature listed in Table 2.2. Although the bottom of the stack was tightened together with stainless steel wire, the entire preform is not fully tacked unless the drop has formed. After the drop falls, the preform is ready to be pulled down the tower to fiber.

All of our final fiber designs required a two stage process to achieve the correct core to clad ratio of $\frac{1}{25}$. During the first step, [see Appendix Figure B.1a] the preform is drawn down to 1.5 mm C-C OD cane. The T_{draw} during the experiment needs to be high enough to allow all of the canes to tack together but also low enough to provide the correct tension. The tension is very important as well because if the T_{draw} is too high then the preform drops faster than the fiber is being pulled. If the T_{draw} is too low though the neck-down can break in the furnace and a restart will be necessary. The T_{draw} difference between the base glass and Er-doped tellurite glass required optimization. The viscosity difference can be seen between the tack quality of the two glass compositions [see Figure 2.13]. We found that to get the correct tension for drawing down to cane we were limited to a narrow draw temperature range of 5°C. The temperature that we drew the tellurite central cane was 535°C [see Table 2.2]. This temperature was much higher than both of the constituent glass cane T_{draw} we

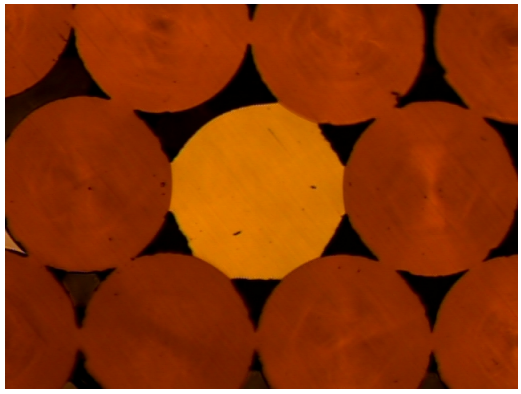

Figure 2.13: Central cane draw for passive tellurite fiber. Lighter central cane is base glass while the darker outer canes are Er-doped tellurite.

Table 2.2: Draw Conditions for Both Tellurite Fiber Steps

Conditions	**Draw Steps**	
	1st Step to Cane	2nd Step to Fiber
Beginning C-C OD (mm)	7.5	7.5
Final C-C OD (μm)	1500	125
Draw Temperature (°C)	535	545
Feed Speed (mm/min)	9.0	2.0
Line Speed (m/min)	0.202	6.3

used but this can also be due to the speed that the glass was being drawn at. The feed speed of the 1st step central cane draw was significantly higher than the initial constituent cane draws. This can cause the glass to have less dwell time in the furnace and therefore will require a higher temperature. The deformation difference between the base glass and the Er-doped glass can be seen in Figure 2.13. This clearly shows that the tellurite glasses have different viscosity values at the same temperature. All of the Er-doped tellurite canes are barely tacked while the base glass tellurite deforms more and provides a stronger tack point.

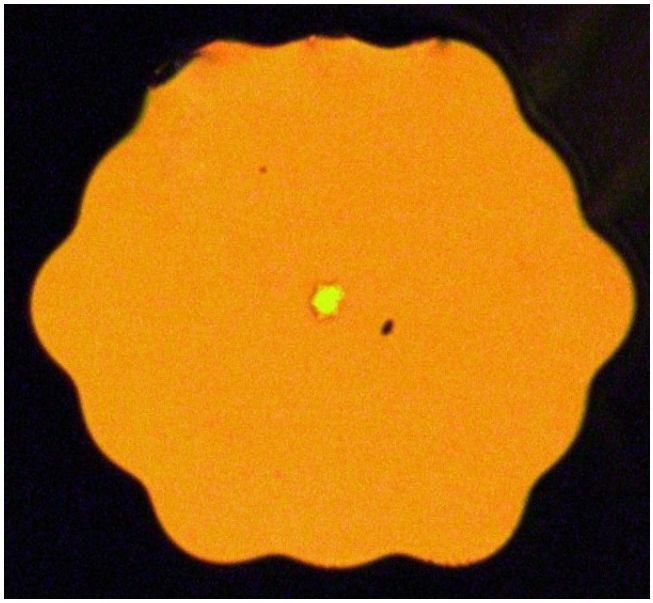

Figure 2.14: Passive fiber for supercontinuum generation with Er-doped tellurite cladding and base glass core (125 μm C-C OD).

Several attempts at the all solid tellurite structure were conducted at both the cane fabrication step and the fiberization step. We discovered that during the central cane production step we needed to tack each of the component rods together and did not have to full consolidate the structure. This step was not necessary until the final fiber was drawn. The final draw step with the 1st-step central cane inserted into the 2nd stack design can be seen in Appendix Figure B.1b. The final tellurite fiber shown in Figure 2.14 was drawn at a temperature of 545°C. The temperature used provided a low enough viscosity to provide the correct tension and acheive a C-C OD of 125 μm. Although this temperature was ideal, the singular cane that did not tack shown in Figure 2.13 also did not fully collapse in the fiber [Figure 2.14]. This was not an issue in the final fiber design because we are only concerned about the nonlinear effect taking place within the core.

After the fabrication of the solid tellurite fiber we decided to move towards a suspended core tellurite structure. Tellurite fibers with an air-cladding have been

investigated extensively [13, 58–63]. The advantage of the air core design is the ability of the ZDW to be changed drastically with the core size. The disadvantage of these designs are the difficulty in fabrication. Several of these designs require highly specialized equipment and call for complicated fabrication methods. These air-cladding fabrication methods rely on using extrusion or preform drilling. The disadvantages, other than high start-up costs, are potential glass contamination from heavy metals.

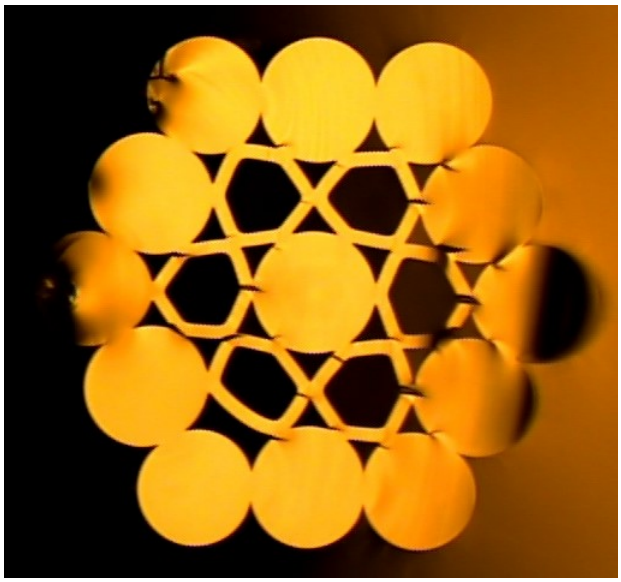

Figure 2.15: Tellurite suspended core cane (1.5 mm C-C OD) drawn down from 7.5 mm C-C OD stack.

This fiber design began by stacking and using the same dimensions as the previously fabricated solid-core tellurite structures (7.5 mm C-C OD) [see Figure 2.12]. To achieve the correct core to clad ratio of $\frac{1}{25}$ we required another two step draw process. Due to the inability in creating an over-clad tube, we were unable to use a pressurized setup. When drawing this preform down to cane, the internal capillary tubes would always collapse. We improved this process by closing off the end of the tellurite tubes in a low temperature furnace by the drop-off method. The tubes

were able to remain open better than previous attempts because the pressure could build up when the bottom of the stack was collapsed. The best cane we were able to produce is pictured in Figure 2.15. This design was unable to be fabricated without a pressurization step so we would have to develop a new approach for fabrication of a suspended core design.

Chapter 3

Tellurite Characterization

A full suite of characterization measurements are necessary to determine the extent of a fiber's capabilities. The refractive index of a glass is an important property to consider when designing a fiber waveguide. The refractive index (RI) is a dimensionless value that provides a numerical relation to the speed of light within a material. Equation 3.1 listed below describes the relationship that RI (n) has with the speed of light in a vacuum (c) and speed of light within a material (v).

$$n = \frac{c}{v} \tag{3.1}$$

The refractive indices that compose an optical fiber are especially important because they need to have the correct ratio between the core and clad to exhibit TIR. This process can be explained by better understanding the refractory behavior of light and therefore Snell's Law (3.2).

$$n_1 \sin(\theta_1) = n_2 \sin(\theta_2) \tag{3.2}$$

Snell's Law allows us to predict a wave of light's interaction with an incident material. This equation can show the refractory effect of light when interacting with a material of differing RI. By rearranging the equation we can get:

$$\sin(\theta_1) = \frac{n_2}{n_1}\sin(\theta_2) \tag{3.3}$$

The critical incident angle of θ_1 can be determined by setting $\sin(\theta_2)$ equal to 1. This translates to θ_2 of 90 °, or when there is no refraction. By defining this value, and knowing your refractive indices of medium 1 and 2, you can determine the incident angle (θ_1) required to provide TIR. Due to the fact that a value of $\frac{n_2}{n_1}$ >1 causes equation 3.3 to be undefined, you know that TIR can not occur at those values. To provide an effective waveguide a higher index core is required.

The RI difference between the core and clad of an optical fiber determines the nonlinear coefficient of the final fiber design. Knowing this information is quite valuable for simulating the waveguide dispersion of a material. This value is extremely important when predicting the nonlinear effects that a certain pulse may introduce to your material. It is imperative to gather as many material properties as possible so that SCG may be simulated with accuracy.

Another important value to quantify within a glass is the fiber loss. Supercontinuum generation from pulsed laser sources typically uses short fiber lengths in the order of several centimeters. This means that fiber loss may not introduce a noticeable restricting effect, but if the fiber loss is in the order of several 10s of dB/m then the broadening can be significantly limited. The spectral broadening in tellurite fibers can be limited if the OH bands caused from water absorption are not controlled properly. This effect is important to characterize before moving on to further testing so limitations can be understood.

3.1 Refractive Index Measurements

The initial RI measurements were conducted using ellipsometry on all three tellurite glasses at J.A. Woolam. We used J.A. Woolam for our ellipsometry measurements because they are a trusted and established company providing ellipsometry measurements. This measurement was completed by combining the data collected from VUV-VASE and IR-VASE instruments. The VUV-VASE can complete spectroscopic ellipsometry from 140 nm to 2.5 μm whereas the IR-VASE can cover from 1.7 μm to 33 μm. Spectroscopic ellipsometry measurements were conducted by using polarized light and changing the angle of incidence upon the glass sample. Whenever the incident light interacts with the glass, a change in polarization state occurs that is acknowledged by the spectrometer. This change in polarization is recognized by an extinction coefficient that can be related to the complex index of refraction. The ellipsometry measurements allowed us to get a broad fit of RI values, ranging from the visible to far-IR for each tellurite glass and helped us to simulate the fiber designs.

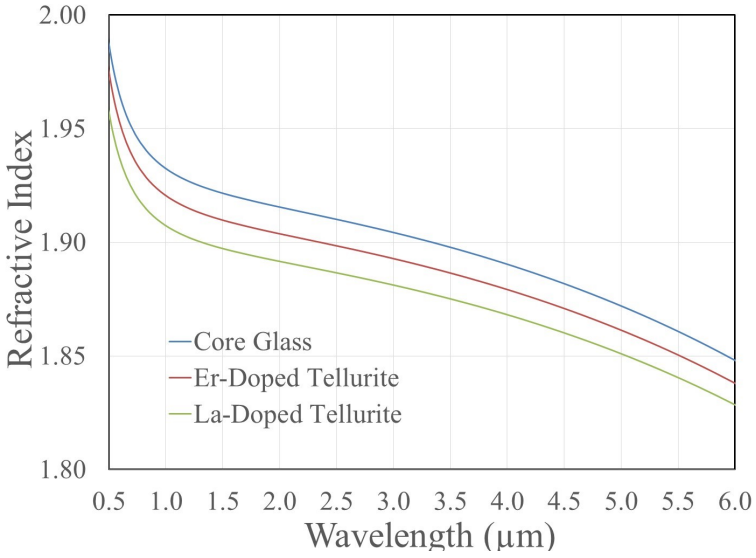

Figure 3.1: Pictured is the refractive index curves for the three different tellurite glass' initial melt designs. The measurements were performed using ellipsometry at J.A. Woolam.

We conducted another set of RI measurements at Clemson University to confirm the indices of the final batch melts. Although we were able to check the pre-melt indices by using ellipsometry, it is very important to confirm the values of the final melt because in a batch melt process glass compositions can change due to a variety of variables. The small button melt samples, shown in Figure 3.2 were measured using prism coupling. Prism coupling is a method of using TIR to confirm refractive index values within thin films or small glass samples [64]. This method requires intimate contact between the prism and the glass sample.

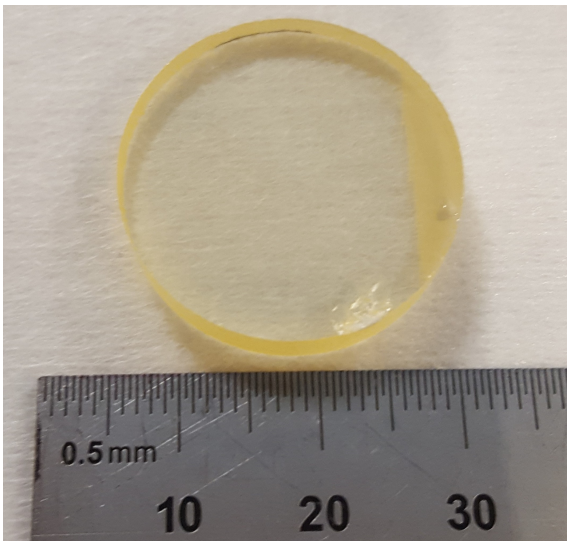

Figure 3.2: A button melt sample of a base glass tellurite melt. This sample is 5 mm thick and was used to measure RI values on the Metricon 2100 prism coupler.

The instrument we used was a Metricon 2010 prism coupler. A higher index prism was required for these measurements because tellurite has such a high RI compared to several thin films and silica glasses that were commonly measured. The button melt sample required a fine polish that was completed by using a step down process with several grit sizes on a rotational polisher. After this process is completed, the glass should be pressed intimately on the prism surface while a pressurized ram is brought in to hold the prism and sample together. The instrument performs the

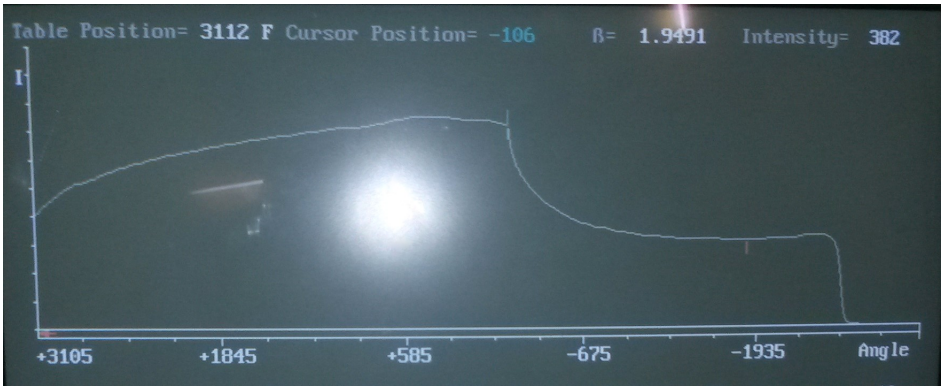

Figure 3.3: Screen illustrating the program used to conduct the Metricon RI measurement. The rapid drop off shown in the transmission curve demonstrates when TIR occurs. This line helps determine the RI of the sample in question from angle of incidence.

measurement by moving circularly around the prism to find the specific angle that provides TIR with the prism and glass surface. The reflection from the glass surface is measured until a drop-off in the transmission occurs [see Figure 3.3]. At this point, the RI can be determined using the RI of the prism and angle of incidence from the beam. Once the indices of the final melts were confirmed, we received the preforms and the fabrication steps began.

3.2 Broadband Loss Measurements

Loss measurements are extremely critical for determining the effectiveness of the supercontinuum generation. The multiphonon edge and the OH absorption band are vital to characterize to determine how far broadening can be extended within a specific waveguide. The reason tellurite and chalcogenides are used for supercontinuum generation is because the multi-phonon absorption edge for both glasses extends beyond 4 μm, unlike fluorides. High loss can be an issue if the glass fabrication process is not controlled carefully and ultra-high purity raw ingredients are not used.

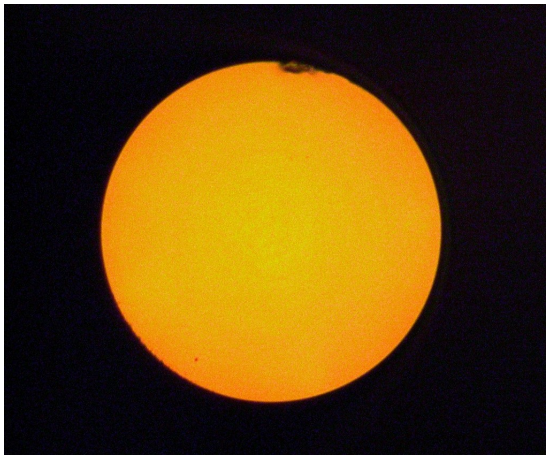

Figure 3.4: Base glass tellurite fiber (125 μm OD) drawn directly from a 1.5 mm cane.

The MWIR loss measurement was conducted on a fiber capable Horiba spectrometer. The multi-detector Horiba iHR320 imaging spectrometer consists of two broadband sources, a monochromator with multiple gratings and filters, and a range of detectors. It has a white light, tungsten source to cover 0.3 - 2 μm and a Globar light source to cover 2 - 15 μm. The system also has 4 detectors: a Thermoelectrically-cooled silicon detector for 0.2 - 1 μm, a liquid nitrogen cooled extended Indium Gallium Arsenic detector for 1 - 1.9 μm, a liquid nitrogen cooled solid-state Indium Antimonide (InSb) detector for 1 - 5.5 μm, and a liquid nitrogen cooled Mercury Cadmium Telluride detector for 2 - 14 μm coverage. The liquid nitrogen is used to cool a detector to increase its accuracy and produce spectroscopic data. The liquid nitrogen causes the thermal excitation of free electrons within the detectors to be reduced which in turn increases accuracy.

The tellurite base glass fiber loss was conducted by first characterizing the handling properties of the fiber. The base glass fiber was stronger than previously drawn soft glass fibers but still could not withstand the clamping force employed with several tension cleavers. Were were able to draw over 50 m of fiber from a 1.5 mm

cane. I utilized a method of hand cleaving to prepare the fibers for the launch set-up. My method began by first dipping the tellurite coated fiber into acetone. After the acrylic coating was swollen slightly in the acetone, I took a scalpel and peeled off the coating gently. When the bare fiber was revealed, I took a small alumina plate and ran it perpendicular to the fiber exterior. This process creates a score on the fiber and allows the material to propagate from that point. Finally, I would pull the fiber tip upwards providing high tension and allowing the fiber to cleave. This hand cleaving method was very repeatable and allowed me to use short fiber sections for measurement. This cleaving method was used for all of my tellurite glass fibers.

We were very concerned with the loss of the bulk glass constituents that were implemented into the final preform design. We achieved this by measuring the individual base glass and Er-doped tellurite glass loss. We also desired to measure the glass loss on the Horiba fiber spectrometer due to the sensitivity that it provided as well as breadth in measurement capabilities. The tellurite glass rods were drawn down from 1.5 mm canes to 125 μm fiber [Figure 3.4]. These two fibers were a solid piece of glass and received no over-clad material except for the acrylic coating. Both fibers were very strong and had slightly higher T_{draw}s than the initial constituent cane draws.

The base glass and Er-doped tellurite glass were both measured so as to provide a full representation of the OH absorption band within the final mictrostructured fiber. Both glasses were measured using the Globar lamp and the InSb liquid nitrogen cooled detector. Each fiber's transmission was measured from 2 μm to 5 μm. The monochromator was used to scan each individual wavelength with a step size of 1 nm. Filters were also used to eliminate higher-order grating reflections. The loss was

gathered by the simple equation listed below:

$$Power(dB/m) = \frac{log(\frac{P_{short}}{P_{long}}) * 10}{Length_{cut}} \tag{3.4}$$

It is easy to convert the loss into dB/m by using a log function and knowing the length that you cutback. This method has been the ideal measurement standard for calculating loss within optical fiber.

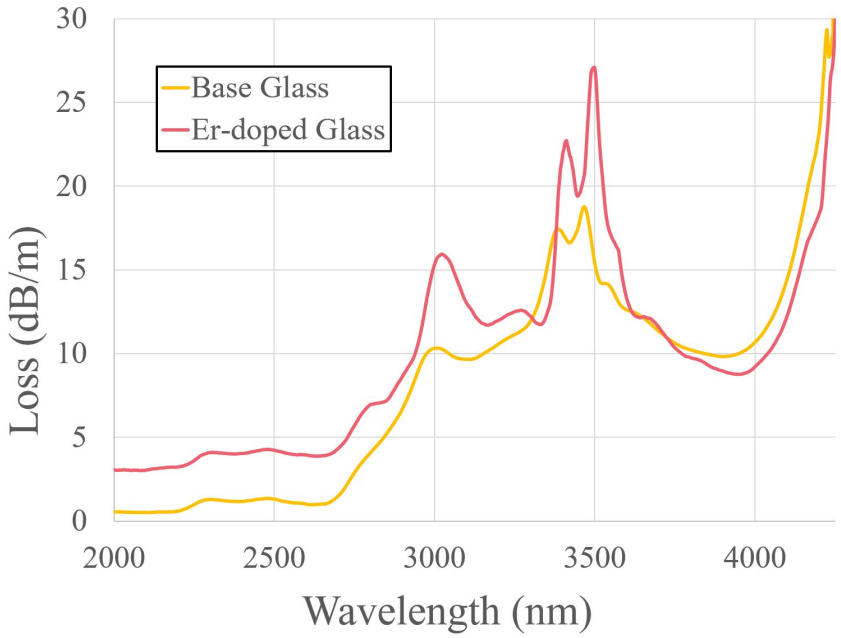

Figure 3.5: Loss measurements conducted on 125 μm OD fibers drawn straight from cane.

The base glass demonstrates a background loss in the fiber <1 dB/m. Figure 3.5 shows that the loss within the base glass reaches a maximum at the water absorption peak of 18 dB/m. This loss value is relatively low compared to other tellurium-barium-zinc glass compositions. The Er-doped tellurite glass though demonstrates a much higher background loss within the fiber reaching 4 dB/m. The peak loss at the water absorption peak is also greater maxing out at approximately 27 dB/m. This

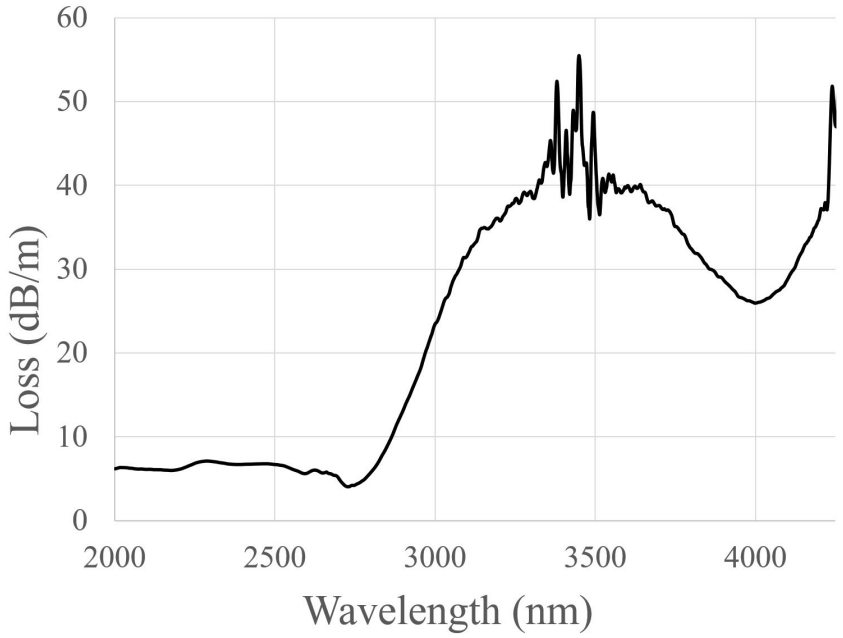

Figure 3.6: Loss measurement conducted on the 125 μm C-C OD passive tellurite fiber used for supercontinuum generation.

higher background loss is most likely caused from the different modifier concentrations [see Table 1.1].

After the stack-and-draw tellurite preform was fabricated, a full loss measurement was conducted to evaluate the losses. Also, gathering the background loss of the constituent canes was important to characterize the loss values of the fabricated fiber. This step is very important because it allows us to gauge the effect on loss that the stack-and-draw process introduces. The measurement shown in Figure 3.6 shows that the background loss of this fiber is around 7 dB/m. Additionally, the loss curve begins a broad absorption band that starts around 2.7 μm and extends to 4 μm. This absorption can be attributed to the OH band within this area and is caused by external water introduced into the system. Although we did go through several drying steps by introducing the entire preform to high heat and increased gas flows. The preform was dried at 200°C with gas flows increased to 5 L/min (5 times higher than

during fiber drawing). The preform underwent 3 passes of drying the entire preform through the hot zone. Although our process was thorough, this method did not keep the interstitial holes between the canes clear from moisture. We had to forgo the use of an over-clad tube because of the difficulty of creating a tube. The over-clad tube during the stack-and-draw process is a useful tool for helping pull the entire preform together without any canes slipping out. We would have benefited most from the use of an outer tube though so that we could pull vacuum on the preform and keep an inert atmosphere. I will go into further methods of reducing the OH absorption band later.

Chapter 4

Dispersion Management

Dispersion is a linear effect that is a major contributor on the influence of several nonlinear interactions within an optical fiber. Dispersion is caused within fiber due to the frequency dependence of the effective index of the guided mode. It can change rather drastically depending on the effects of the waveguide and material dispersion influence.

Phase velocity and group velocity are both effected by dispersion in the context of supercontinuum generation and both should be considered. The phase matching conditions of the fiber contribute significantly to the frequency conversion process of the fiber and should be taken into careful consideration when designing a nonlinear fiber. The higher order dispersion terms along with the group velocity dispersion is quantified by the coefficients contained in the Taylor series expansion of the propagation constant. GVD can be defined by two widely accepted ways: β_2 with units (s^2m^{-1}) and D = -$(2\pi c/\lambda^2)\beta_2$ with units (ps nm^{-1} km^{-1}).

There are two dispersion regimes in medium, the normal dispersion regime D $<$ 0 and the anomalous dispersion regime D $>$ 0. The point in which D = 0 is referred to as the ZDW. A fiber may exhibit multiple ZDWs depending on the waveguide

structure [59]. Even without the effects of nonlinearity, an input pulse will experience broadening due to the effect of the dispersion. By introducing nonlinearities to the system a pulse can be shaped depending on the sign of the dispersion. In the coming sections I will discuss the effect that pump wavelength and dispersion had on the supercontinuum generation.

4.1 Simulating the Dispersion Profiles of the Tellurite Fiber Designs

Simulating an optical fiber's waveguide dispersion is conducted numerically. Also, within the simulations that we conduct, we only take into account the chromatic dispersion and not the polarization mode dispersion or intermodal dispersion due to the fact that single-mode fiber is assumed. The refractive index data obtained from the ellipsometry measurements [see Figure 3.1] was used for determining the fiber dispersion using a homemade fiber mode solver.

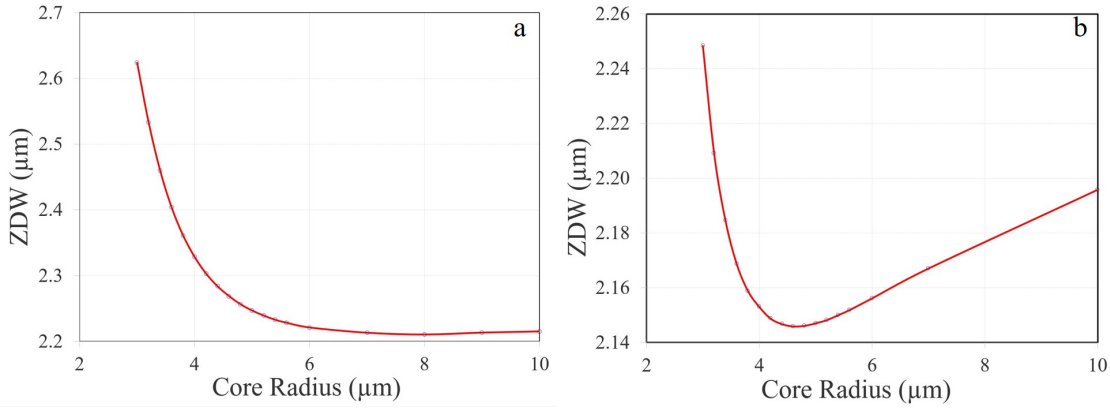

Figure 4.1: ZDW designs for: a) Er-doped tellurite clad; b) La-doped tellurite clad.

The ZDW versus core diameter is summarized in Figure 4.1(a). This model shows the rigidity in design by using the base glass as the core and Er-doped tellurite

as cladding. With the current refractive index contrast between the core and cladding, the minimum ZDW is 2210nm. For supercontinuum generation, it is better to have the pump wavelength located near the ZDW and in the anomalous dispersion regime. In our case with a Tm-doped fiber laser pump, this implies a ZDW of 1.9μm. This target is not achievable with the current cladding material and a lower cladding index is required to achieve this objective. The core diameter of 5μm was chosen because it provided flattened dispersion even though the ZDW was not optimal.

We also simulated our original design with La-doped tellurite cladding [Figure 4.1(b)]. Although this fabrication process was not feasible, we wanted to provide the dispersion design. This design clearly shows that by increasing the contrast between the RI of the core and clad, a lower ZDW is possible.

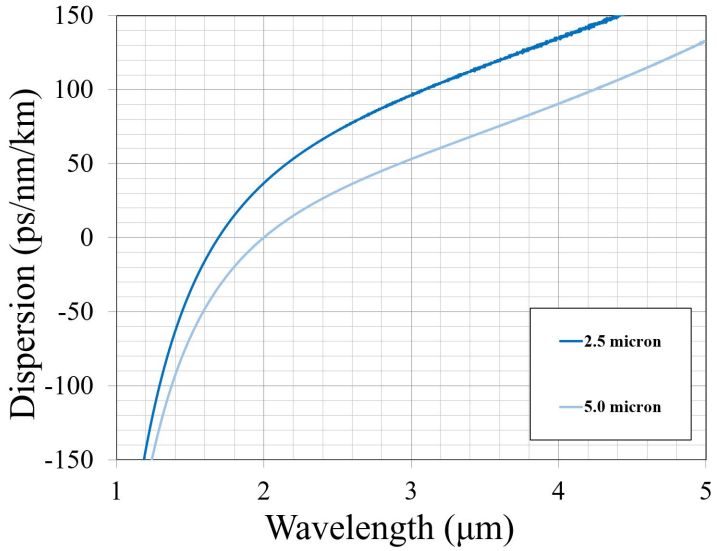

Figure 4.2: Dispersion profiles of the air-cladding design with respective core radius denoted.

It was also necessary to demonstrate the potency of suspended core designs and their effectiveness at altering the ZDW. We demonstrated that by using the same base glass as a core the ZDW could be changed with much greater ease than

our all-solid designs. The air-cladding provides such a large difference in RI over other tellurite glasses that the waveguide dispersion is increased significantly. Using our home-made fiber solver we showed that just by changing the fiber's core radius from 2.5 μm to 5.0 μm the ZDW could be altered from 1.64 μm to 2.0 μm respectfully. This dispersion altering can be a huge aid to increase broadening by pumping in the anomalous dispersion regime.

4.2 Measuring the Tellurite Fiber Dispersion

After the loss was calculated, a good estimate of the correct length to use for dispersion measurements was determined. Dispersion of a fiber is critical for efficient supercontinuum generation. A great deal of effort has been made to alter fibers by photonic crystal structures or core size adjustments to move the ZDW to the pump wavelength [13, 58, 62, 65]. By using a stack-and-draw method, fiber design can be controlled with ease. Studies have demonstrated that by adjusting the core size within a micro-structured PCF one can modify the ZDW significantly. Increasing the core size in a tellurite "wagon wheel" structure from 1.1μm to 4.2μm moves the ZDW from 977 nm to 1547nm respectively [65].

Low coherent interferometry was used for the dispersion measurements. Interferometry using a bright white light source is an effective an accurate method of measuring group delay down to the fs level accuracy [66]. A supercontinuum source with a single-mode delivery fiber from 650 to 2300nm was used to cover a wide wavelength range. The input beam is split into two arms of the interferometer. The path length of the reference arm can be adjusted to coincide with the designated fiber length. The tellurite fiber was placed at the measurement arm. Beams from the two arms were combined and then passed through a monochromator for wavelength

selection. The coherent interference was measured with a liquid-nitrogen-cooled InSb detector.

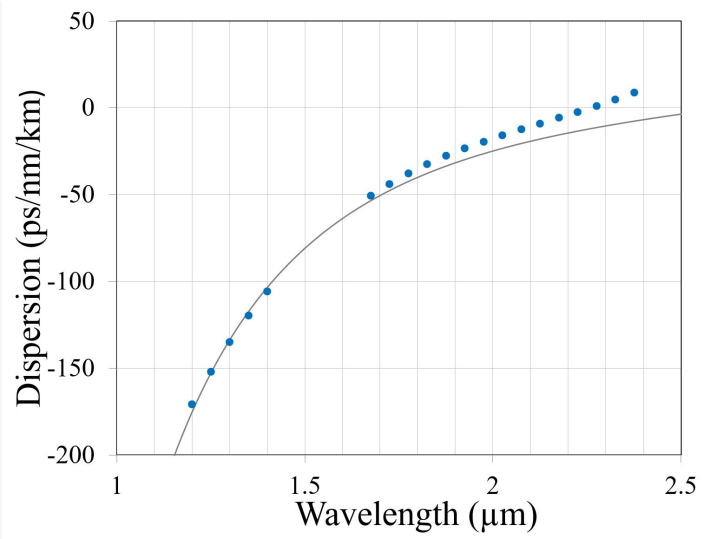

Figure 4.3: Passive tellurite fiber design with measured dispersion (dots) and simulated dispersion (line).

The reference arm path length was roughly chosen for the fiber length initially and is then finely adjusted. Small step sizes from a motorized linear translational stage are used to determine the exact location for coherent interference. This was performed for a range of wavelengths to gather the delay-versus-wavelength data for the tellurite fiber. Due to the erbium-doped nature of the cladding, data collection near 1 μm and between 1.4 - 1.6 μm was not possible due to erbium-absorption. A polynomial fit was first performed on the delay-versus-wavelength data. The dispersion data can then be obtained from the polynomial fit by taking a simple derivative. The measured dispersion is similar to the simulation [see Figure 4.3]. The measured ZDW is 2260nm.

Chapter 5

Supercontinuum Generation

Nonlinear optics is a field that has been studied to a great extent but until recently has been underutilized. Nonlinear optics refers to any optical effect that occurs when output power does not scale accordingly to the input power that is introduced to a system. Nonlinear effects are not usually a concern at low intensities but can be an issue at high peak powers. Depending on your application though, nonlinear effects can be utilized from broadening of an input pulse, to demonstrating lasing.

Nonlinear optics were not investigated until the discovery of the laser in 1960 [44]. Prior to the invention of the laser, there were no light sources capable of causing nonlinear effects and therefore it was never explored. The discovery of second-harmonic generation in 1961 opened up the flood-gates for a decade of discovery in nonlinear optics. Although the field was growing at a rapid rate, nonlinear optics within an optical fiber could not be investigated due to significant losses. This all changed with the discovery of the chemical vapor deposition process and consequently low loss fiber at Corning in 1970.

SCG is a unique method of producing bright, broad spectral bandwidth sources.

SCG is unique because it is a process that uses the nonlinear effects in a material to cause spectral broadening from a narrow linewidth laser in a medium. SCG is an instance of using nonlinear effects for a positive application.

5.1 Measuring Supercontinuum Generation

The supercontinuum generation experiment was conducted using a Thulium doped femtosecond fiber laser (Thorlabs FS-1900) as the pump source. The laser consists of a seed oscillator at 50 MHz repetition rate with a tunable center wavelength between 1900nm and 1960nm, and a Thulium doped fiber amplifier for boosting the oscillator power to $>$ 500 mW. The laser output was collimated and focused onto the cleaved facet of the tellurite fiber using an aspheric lenses. The output light from the tellurite fiber was collimated using a MWIR transparent aspheric lens and was coupled into a MWIR capable Fourier-transform spectrum analyzer (Thorlabs OSA205).

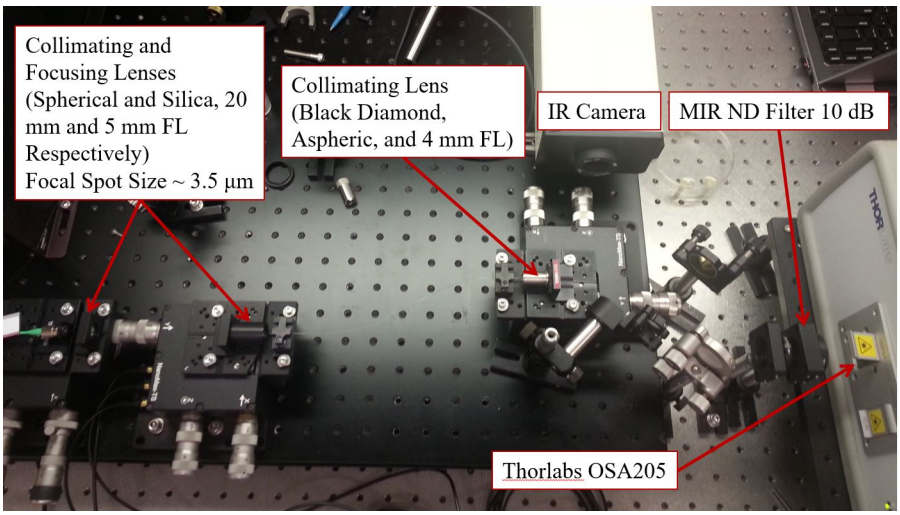

Figure 5.1: The supercontinuum measurement setup at Thorlabs Quantum Electronics.

First, the seed oscillator wavelength and the amplifier dispersion were adjusted

in order to determine the optimal conditions that maximize the supercontinuum spectrum in a tellurite fiber sample with fixed length. The next step was to test for the ideal length of fiber that balanced nonlinear effects and fiber loss. The length decided upon was 60 mm for the tellurite fiber. Various lengths of fiber were tested [see Figure 5.2(a)] but often in highly nonlinear fibers, the broadening is maxed out at centimeter lengths. The pump laser provided a center wavelength of 1949 nm, a pulse duration of 52 fs, and an average power of 570 mW.

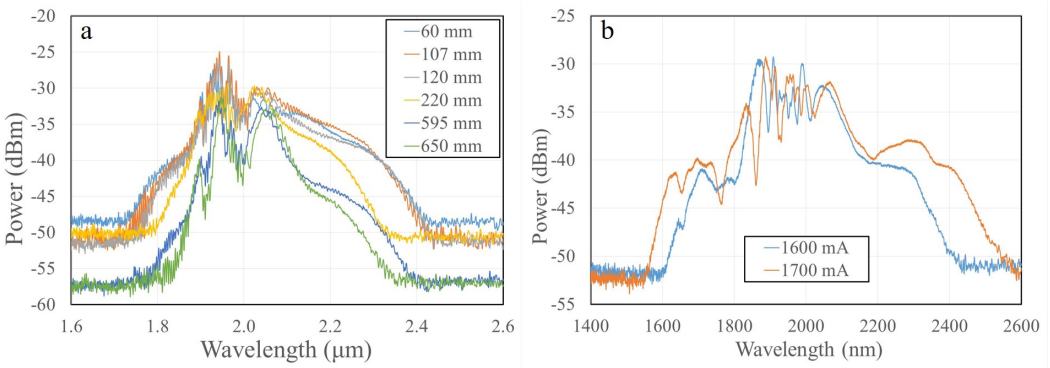

Figure 5.2: Demonstration of the supercontinuum generation optimization: a) Graph showing the effect of fiber length on broadening; b) Graph demonstrating the increase in broadening from just a small increase in pump.

Approximately 1000 nm of spectral broadening was measured [see Figure 5.3]. Although the laser's central wavelength is over 300 nm from the ZDW, we were still able to obtain supercontinuum generation from 1.6 - 2.6 μm. The conversion efficiency from pump to supercontinuum is much higher than the previous mid-IR supercontinuum generation in a tellurite fiber [3, 12]. The relative power difference of the pump at 1949 nm and supercontinuum is less than 10 dB.

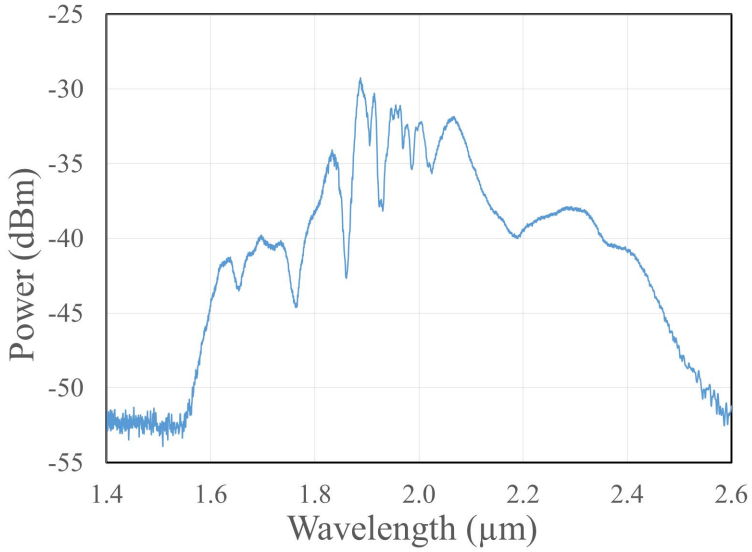

Figure 5.3: Supercontinuum generation with 60 mm fiber length.

5.2 Simulating the Tellurite Fiber Supercontinuum

A simulation was conducted for this fiber using the SCG code provided within Dudley et al. [67]. The code was intended for use with silica fibers therefore various parameters were altered for our tellurite fibers. The code can be seen within Appendix A. An estimated peak power of 20 kW was used. The nonlinear index (n^2) used was 2.5×10^{-19} m^2/W [53]. Raman effects were also incorporated. Due to the lack of measured Raman data for tellurite, Raman data for silica is used (f_r=0.18, τ_1=0.0122 ps, τ_2=0.032 ps) [67]. Raman processes are responsible for the wavelength shift of solitons in the anomalous dispersion regime. This is not significant in this demonstration since most of the supercontinuum is in the normal dispersion regime. This can lead to errors for significant soliton propagation in the anomalous regime. By using silica Raman data, we may be underestimating the broadening that can occur in the anomalous dispersion regime. Further work is required to characterize Raman parameters for tellurite. The dispersion used was from simulated dispersion

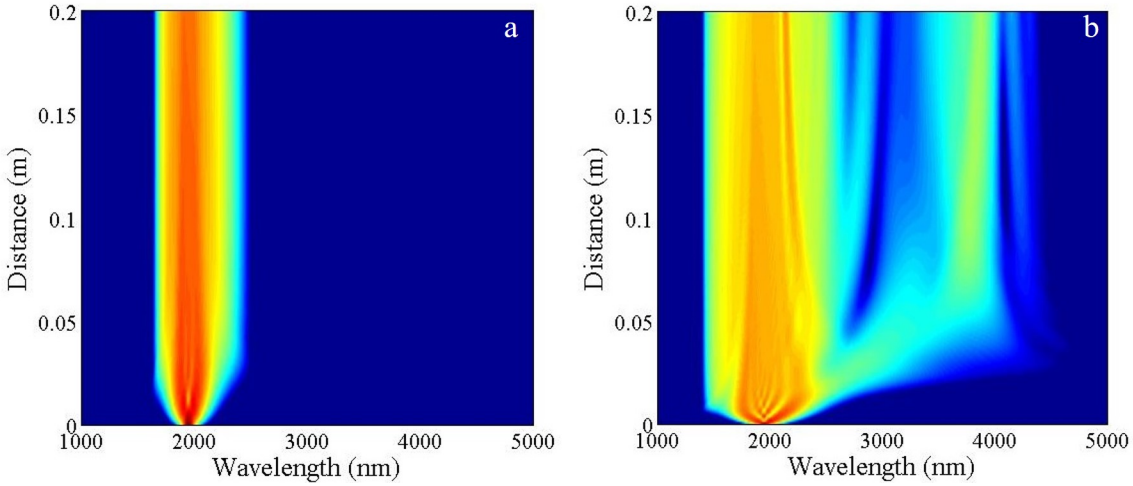

Figure 5.4: Simulated supercontinuum generation with an Er-doped tellurite cladding: a) 20 kW peak power; b) 100 kW peak power.

data (β_2=0.057575 ps^2/m, β_3=1.607x10^{-4} ps^3/m, β_4=-2.41x10^{-7} ps^4/m). Due to the constraint of the current program, we cannot use a wavelength dependent nonlinear coefficient or loss. The constant nonlinear coefficient (γ) of 0.02095 1/m/W and loss of 6 dB/m was used. These constraints can be removed in the future to better estimate the supercontinuum generation.

The simulated supercontinuum is shown in Figure 5.4(a) and is very close to the measured supercontinuum for 60 mm and 107 mm long fibers. Since the pump wavelength is located in the normal dispersion regime, most spectral broadening occurs initially from the self-phase modulation (SPM). The tellurite fiber's high nonlinearity makes SPM very efficient. The clear cut-off on the near IR side is due to increasing normal dispersion towards shorter wavelengths. Soliton formation and related wavelength shifts can also be observed in the anomalous regime (>2.3 μm). Simulation is also performed for 100 kW peak power [see Figure 5.4(b)] which shows that a significantly broader supercontinuum can be achieved at higher powers. Multiple soliton formations in the anomalous regime can be observed in this case above

2.3 μm.

Additional simulations were also performed at 20 kW and 100 kW for a fiber with a La-doped tellurite cladding. This fiber was our original fiber design so we wanted to demonstrate the effect that lower dispersion presented in reference to supercontinuum generation. All the other parameters between the fibers were kept the same except the nonlinear coefficient (γ) of 0.0357 1/m/W and dispersion data (β_2=0.03316 ps^2/m, β_3=2.23x10^{-4} ps^3/m, β_4=5.08x10^{-7} ps^4/m). The result is shown in Figure 5.5(a) and (b). It can be seen that the overall flattened dispersion significantly broadened the supercontinuum. This is interesting and was unexpected. The high nonlinearity of tellurite fiber leads to significant spectral broadening through SPM in the normal dispersion regime. This produces considerable power in the anomalous dispersion regime after a very short propagation, which in turn leads significant spectrum broadening through soliton effects in the anomalous dispersion regime. This unforeseen effect makes moving the ZDW to the pump wavelength less important. It needs to be noted that although lower dispersion can be obtained

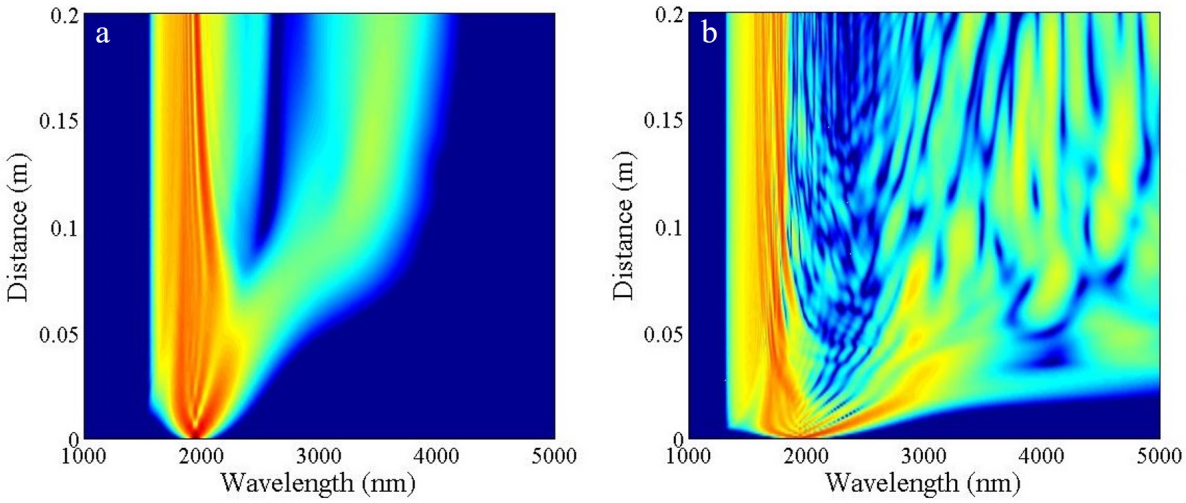

Figure 5.5: Simulated supercontinuum with a La-doped tellurite cladding: a) 20 kW peak power; b) 100 kW peak power.

with smaller core diameters, such fibers become very weakly guided above 3 μm [58]. This can lead to a significant mode area increase and consequently lower nonlinear coefficient with an increase of wavelengths above 3 μm.

As a comparison, we further studied designs with cladding made of air to lower the ZDW and improve the waveguide. This can be achieved by any number of the suspended core designs [11, 13, 58, 60–63, 65, 68, 69]. This increased refractive index contrast between core and cladding in this case leads to a much higher waveguide dispersion which can be used to compensate for material dispersion. A much wider shift of the ZDW can be obtained in this case [65]. For a design with the base glass as a core material and with air as cladding, the fiber dispersion was simulated and shown in Figure 4.2 with two core radii. Due to this higher waveguide dispersion, a much broader range of ZDWs can be obtained by slight adjustments in core size. We executed the supercontinuum simulation again for the air clad design with a core diameter of 4 μm at 20 kW and 100 kW peak powers, keeping all parameters the same except the nonlinear coefficient (γ) of 0.0361 1/m/W and dispersion data (β_2=-7.02x10^{-3} ps^2/m, β_3=2.95x10^{-4} ps^3/m, β_4=-8.147x10^{-5} ps^4/m) [see Figure 5.6]. This

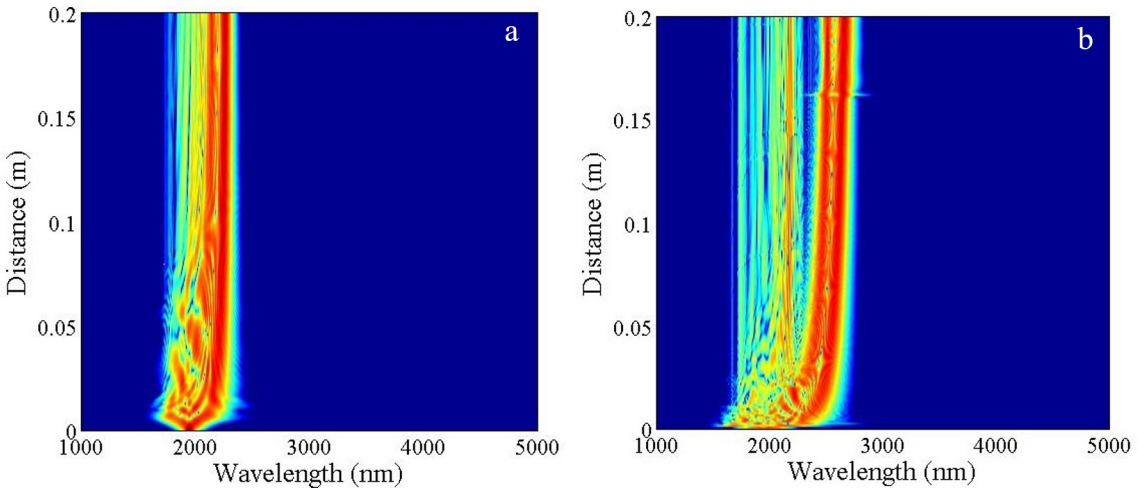

Figure 5.6: Simulated supercontinuum with a suspended core tellurite structure: a) 20kW peak power; b) 100kW peak power.

fiber design demonstrated a ZDW of 1918nm just slightly below the pump wavelength at 1949nm in the normal dispersion regime. It is surprising to see the simulated supercontinuum is not as broad as within the La-doped tellurite-clad fiber. This is due to the higher dispersion of this fiber in the anomalous dispersion regime seen in Figure 4.2. This simulation demonstrates that lowered/flattened dispersion and not the ZDW is a more important factor for supercontinuum generation in tellurite fibers pumped at 2 μm.

Chapter 6

Conclusion

In conclusion, we have demonstrated a simple and flexible stack-and-draw fabrication process for an all-solid tellurite fiber. In this fabrication process, we have shown that design and implementation of a solid tellurite fiber is easily manipulated and requires a small amount of raw materials. Additionally, we have proven that fabricating a stack-and-draw preform is entirely possible without the need for an over-clad tube. Using this simple process allows for inexpensive fabrication of complex preforms and requires simple preparation and equipment. Several other soft glass fiber designs for supercontinuum generation required a soft glass tube or capillary at one point or another. This fabrication design eliminates using the rod-in tube method, complicated pressure setups, expensive extrusion, or core-drilling processes.

We have conducted both loss and dispersion measurement of the fabricated tellurite fiber, demonstrating sufficiently low losses for supercontinuum generation. We have also demonstrated supercontinuum from 1.6 - 2.6 μm in the fabricated fiber. This is achieved despite pumping in the normal dispersion regime and slightly far away from the ZDW. The efficiency is due to the significant SPM induced spectral broadening. This broadening is a result of high nonlinearity in tellurite fibers, and

a much lower dispersion between 2 - 4 μm in all-solid designs. A broadening of the supercontinuum from 1.5 - 4 μm can be generated in the same fiber with a higher pump power laser. Additionally, a similar fiber with a slightly improved refractive index difference between core and cladding can demonstrate broadening from 1.5 - 5 μm if OH absorption losses are controlled. We have further demonstrated that lower dispersion in the anomalous regime, not ZDW location, is more important for efficient supercontinuum generation pumped at 2 μm. This would imply that a solid design is superior to a micro-structured design for supercontinuum generating tellurite fiber. The improved bandwidth is due to the rapid SPM spectral broadening as a result of the high nonlinearity in tellurite fibers. This leads to significant power in the anomalous dispersion regime after only a short propagation.

The new stack-and-draw process reported in this work demonstrates a simple and flexible process with a reduced risk of contamination. Despite the fact that the desired high-power broadband MWIR supercontinuum generation has not been achieved, this work has clearly identified optimal designs and a fabrication process with which to move forward.

6.1 Future Work

Although the supercontinuum simulations are not representative of the supercontinuum broadening that we are looking for, better control of waveguide dispersion can be expected to improve the simulations. The suspended core structure provides a level of control in the zero dispersion wavelength that the solid fiber designs can not provide. The reason this occurs is due to the sharper difference between the core and clad refractive indices. We would like to implement this design without the use of tellurite tubes while also keeping the fabrication method very simple.

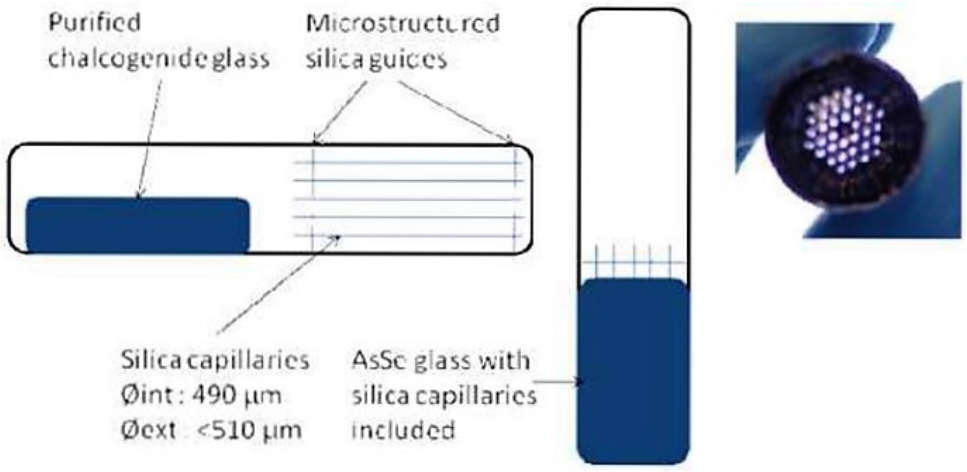

Figure 6.1: This melt design demonstrates the ability for a micro-structured soft glass design to be made without using soft glass tubes, extrusion, or core drilling [70].

We are basing much of our future core rod fabrication design on a paper sumbitted by Coulombier et. al [70]. The foundation of this work revolves around creating a micro-structured air-clad soft glass design. This fabrication method is implemented without using any soft glass tubes but rather thin silica capillaries to create the suspended core structure. Silica tubes are readily available and are much easier to produce than soft glass tubes. By implementing a process with just soft glass rods and silica tubes, a melt design can be created very inexpensively and easily.

The coefficient of thermal expansion difference between many soft glasses and silica is rather large. This paper implements the use of an As_2Se_3 chalcogenide soft glass with thin wall silica capillaries. As_2Se_3 and TeO_2 glasses have very similar α_{th} and therefore interface physical interactions with silica should be similar. Both glasses exhibit a α_{th} of approximately $20x10^{-6}$ $^{\circ}C^{-1}$. They have proven that by using silica capillaries with a internal diameter to OD ratio of 0.96 that the capillaries will mitigate stress caused by thermal expansion differences. This process is very crucial, and they have shown that even slight variation in wall thickness of a couple microns can cause thermal stress cracking.

To begin our process, we will use our base glass tellurite rods and form them within a similar stack-and-draw structure as previous suspended core designs. The interior tellurite tubes shown within Figure 2.12 will be replaced by 0.96 ratio silica tubes. The difference with this design is that it will be wrapped within platinum foil to allow for an easy removal process. Platinum foil is an inert metal and does not leech into or stick onto the glass. We have tested this by performing small melt experiments with both platinum and gold foil and noticed a reasonable discoloration with gold foil. Discoloration occurs within the areas of contact with the glass which proves, that some leeching has taken place.

Whenever the glass has finished within its melt design, we will have a air-clad tellurite structure with silica capillaries creating a suspended core. The silica capillaries were shown to be easily etched away with HF acid. This work showed no negative effects towards the chalcogenide glass. Tellurite glass resists acidic attack greater than chalcogenide glass so we can expect to see no negligible effects towards the preform. Silica glass has defined HF etch rates therefore glass with a 30 μm wall will be easily removed.

The crucible we will use will be silica rods arranged in a hexagonal stack arrangement to provide a familiar shape. By using the stacking process to create our crucible container, we can construct the dimensions we desire making the entire process very flexible. The entire melt designed preform will be fabricated within hexagonal support clamps. The rigidity and ease of fabrication makes this a very efficient design.

Using this melt process to melt the interior rod will also mitigate many of the issues introduced by not implementing a clad tube in the stack-and-draw process. With the glass melt in any inert atmosphere, the material should exhibit significantly lower OH absorption. The material once melted together in the correct structure

should also be very easy to implement into our familiar stack-and-draw design process. This melted central cane will exhibit much lower losses and will be stacked again to achieve the $\frac{1}{25}$ core clad ratio that we desire. Although we will be going through the stack and draw process again, by melting the central cane the preform around the core will be fully consolidated. Due to this fact we will not have to worry about introducing any water losses into the core area where supercontinuum generation will occur.

Another area of improvement will be the mitigation of OH loss within our tellurite glass at the 2.7 - 4.0 μm band. One approach for solving this issue is by using halide binary ingredients rather than oxides. During glass formation, the tellurite bonds with the other glass modifiers such as Zn- and Ba-, but the oxide additions are occasionally left free. This causes them to attach to any open hydrogen available in the system. This OH bond will then be left in the glass structure. If halide additions are added into the system such as chlorides or fluorides (Zn-F_2, -Cl_2 or Ba-F_2, -Cl_2) then the free hydrogen will attach to these halides and will be significantly more volatile than -OH and likely to leave the system. The effects of fluoride and chlorinated glasses have been explored in detail and with significant results [3, 12, 27, 31, 68, 69, 71, 72] While it is evident that halides do provide dehydration, they should be introduced in small amounts. If the concentration is not controlled in relation to oxide additions then crystallization can occur [22].

Appendices

Appendix A Supercontinuum Generation Code

Supcontinuum Code Written by J.C. Travers, M.H. Frosz, and J.M. Dudley (2009)
Refer to Chapter 3 of Reference [67]

Altered for Fabricated Tellurite Fiber

```
%Simulate supercontinuum generation
n = 2^13;                                   % number of grid points
twidth=12.5;                                %width of time window [ps]
c=299792458*1e9/1e12;                       %speed of light [nm/ps]
wavelength=1949;                            %reference wavelength [nm]
w0=(2.0*pi*c)/wavelength;                   %reference frequency [2*pi*THz]
T=linspace(-twidth/2, twidth/2, n);         %time grid
% === input pulse
power=20e3;                                 %peak power of input [W]
t0=0.052;                                   %duration of input [ps]
A=sqrt(power)*sech(T/t0);                   %input field [W^(1/2)]
% === fiber parameters
flength=0.2;                                %fiber length [m]
%betas = [beta2, beta3, ...] in units of [ps^2/m, ps^3/m, ...]
betas = [5.7575e-2, 1.607e-4, -2.41e-7, 0, 0]; %[57.575, 0.1607, -2.41e-4, 0, 0]
gamma=0.02095;                              %nonlinear coefficient [1/W/m]
loss=6;                                     %loss [dB/m]
% === Raman response
fr=0.18;                                    %fractional Raman contribution
tau1=0.0122; tau2=0.032;
RT=(tau1^2+tau2^2)/tau1/tau2^2*exp(-T/tau2).*sin(T/tau1);
RT(T<0)=0;                                  %heavyside step function
RT=RT/trapz(T,RT);                          %normalise RT to unit integral
% === simulation parameters
nsaves=200;                                 %number of length steps to save field at
%propogate field
[Z, AT, AW, W] = GNLSE_function_code(T, A, w0, gamma, betas, loss, fr,
RT, flength, nsaves);
% === plot output
figure();
lIW=10*log10(abs(AW).^2);                   %log scale spectral intensity
mlIW=max(max(lIW));                         %max value, for scaling plot
WL=2*pi*c./W; iis=(WL>1000 & WL<5000);      %wavelength grid
subplot(1,2,1);
```

```
35  pcolor(WL(iis), Z, lIW(:,iis));                    %plot as pseudocolor map
36  caxis([mlIW-40.0, mlIW]); xlim([1000,5000]); shading interp;
37  xlabel('Wavelength (nm)');
38  ylabel('Distance (m)');
39  lIT=10*log10(abs(AT.^2));                          %log scale temporal intensity
40  mlIT=max(max(lIT));                                %max value, for scaling plot
41  subplot(1,2,2);
42  pcolor(T, Z, lIT);                                 %plot as psuedocolor map
43  caxis([mlIT-40.0, mlIT]); xlim([-0.5,5]); shading interp;
44  xlabel('Delay (ps)');
45  ylabel('Distance (m)');
```

Appendix B 3-D Preform and Clamp Designs

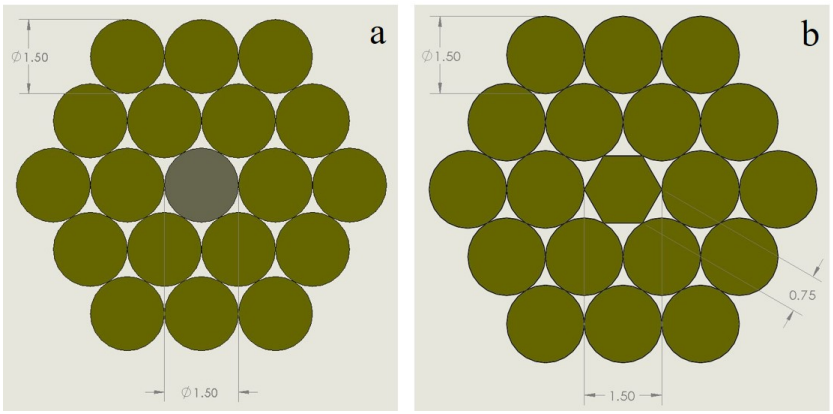

Figure B.1: Tellurite SCG fiber stack design steps: a) First stack design step (step 1) showing base glass as the central cane and Er-doped tellurite glass as the cladding. This design was drawn down to a 1.5 mm C-C cane.; b) Second stack design step (step 2) showing the hexagonal cane drawn from step 1 [see Figure B.1(a)] in the center surrounded by two rows of Er-doped tellurite glass. This stack was drawn down to 125 μm fiber.

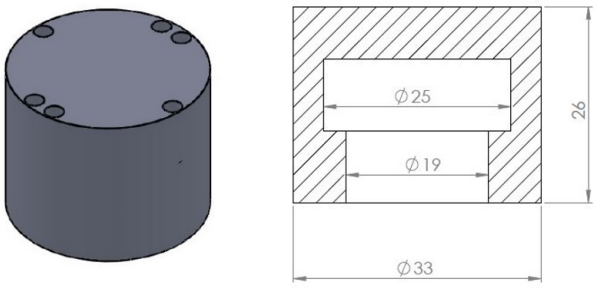

Figure B.2: Depiction of the clamp used to grasp the Kigre rod preforms pictured in Figure 1.8. The clamp was split in two and surrounded the preform "nub". This clamp was then attached to a long stainless steel rod that extended through the furnace and was tightened into the glass chucks. This process allowed us to draw the entire preform without worrying about limited chuck distance to the furnace.

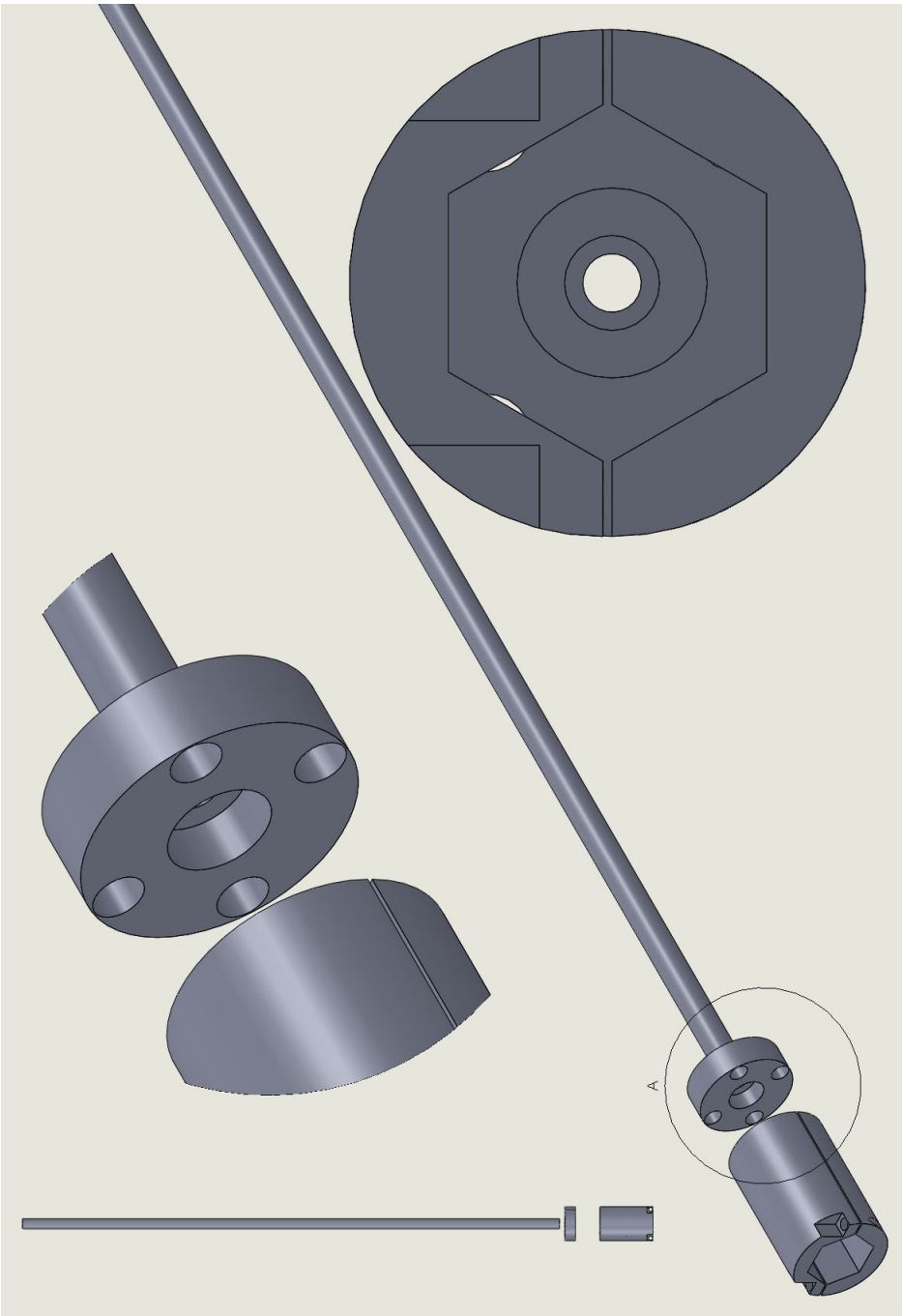

Figure B.3: Depiction of the clamp setup used to draw each of the stack designs pictured in Figure B.1. There were four seperate pieces: 1) Bottom clamp; 2) Top Clamp; 3) Combining piece; 4) Handle rod. By using this clamp design, we were able to utilize an entire preform while it remained in the furnace. This was useful because there is a large temperature difference between the outside atmosphere and the inside of the furnace. If this was not controlled then the preform could experience thermal shock.

Bibliography

[1] Manijeh Razeghi, Steven Slivken, Yanbo Bai, and Ramezani Darvish. The quantum cascade laser: A versatile and powerful tool. *Optics and Photonics News*, 19(7):42–47, 2008.

[2] Gail Overton. Ir countermeasures aim for safer flights. *Laser Focus World*, 47(8), 2011.

[3] Dan L. Rhonehouse, Jie Zong, Dan Nguyen, Rajesh Thapa, Kort Wiersma, Chris Smith, and Arturo Chavez-Pirson. Low loss, wide transparency, robust tellurite glass fibers for mid-ir (2 - 5 um) applications. volume 8898, pages 88980D–88980D–8.

[4] M. Vainio and L. Halonen. Mid-infrared optical parametric oscillators and frequency combs for molecular spectroscopy. *Phys Chem Chem Phys*, 18(6):4266–94, 2016.

[5] Matthew Barre and Eric Takeuchi. Breath analysis research approaches clinical practicality. *Laser Focus World*, 49(4), 2013.

[6] R. R. Alfano and S. L. Shapiro. Observation of self-phase modulation and small-scale filaments in crystals and glasses. *Physical Review Letters*, 24(11):592–594, 1970.

[7] Émilie Du Châtelet. Dissertation sur la nature et la propagation du feu: An essay on heat. 1744.

[8] Edvige Schettino. A new instrument for infrared radiation measurements: the thermopile of macedonio melloni. *Annals of Science*, 46(5):511–517, 1989.

[9] J.H. Taylor and H.W. Yates. Infrared transmissions of the atmosphere, 1960.

[10] Charles W. Rudy. Power and pulse capability ramp up for mid-ir lasers. *Laser Focus World*, 50(5), 2014.

[11] P. Domachuk, N. A. Wolchover, M. Cronin-Golomb, A. Wang, A. K. George, C. M. B. Cordeiro, J. C. Knight, and F. G. Omenetto. Over 4000 nm bandwidth of mid-ir supercontinuum generation in sub-centimeter segments of highly nonlinear tellurite pcfs. *Optics Express*, 16(10):7161–7168, 2008.

[12] Rajesh Thapa, Dan Rhonehouse, Dan Nguyen, Kort Wiersma, Chris Smith, Jie Zong, and Arturo Chavez-Pirson. Mid-ir supercontinuum generation in ultra-low loss, dispersion-zero shifted tellurite glass fiber with extended coverage beyond 4.5 μm. volume 8898, pages 889808–889808–8.

[13] Meisong Liao, Xin Yan, Guanshi Qin, Chitrarekha Chaudhari, Takenobu Suzuki, and Yasutake Ohishi. A highly non-linear tellurite microstructure fiber with multi-ring holes for supercontinuum generation. *Optics Express*, 17(18):15481–15490, 2009.

[14] Christian Rosenberg Petersen, Uffe Moller, Irnis Kubat, Binbin Zhou, Sune Dupont, Jacob Ramsay, Trevor Benson, Slawomir Sujecki, Nabil Abdel-Moneim, Zhuoqi Tang, David Furniss, Angela Seddon, and Ole Bang. Mid-infrared supercontinuum covering the 1.4-13.3 um molecular fingerprint region using ultra-high na chalcogenide step-index fibre. *Nat Photon*, 8(11):830–834, 2014.

[15] L. Pauling, A. B. Robinson, R. Teranishi, and P. Cary. Quantitative analysis of urine vapor and breath by gas-liquid partition chromatography. *Proc Natl Acad Sci U S A*, 68(10):2374–6, 1971.

[16] Michael J. Thorpe, David Balslev-Clausen, Matthew S. Kirchner, and Jun Ye. Cavity-enhanced optical frequency comb spectroscopy: application to human breath analysis. *Optics Express*, 16(4):2387–2397, 2008.

[17] M. Phillips, M. Sabas, and J. Greenberg. Increased pentane and carbon disulfide in the breath of patients with schizophrenia. *Journal of Clinical Pathology*, 46(9):861–864, 1993.

[18] Robert Stegeman, Ladislav Jankovic, Hongki Kim, Clara Rivero, George Stegeman, Kathleen Richardson, Peter Delfyett, Yu Guo, Alfons Schulte, and Thierry Cardinal. Tellurite glasses with peak absolute raman gain coefficients up to 30 times that of fused silica. *Optics Letters*, 28(13):1126–1128, 2003.

[19] G. W. Brady. X-ray study of tellurium oxide glass. *The Journal of Chemical Physics*, 24(2):477–477, 1956.

[20] A. Winter. Glass formation. *Journal of the American Ceramic Society*, 40(2):54–58, 1957.

[21] N. Mochida, K. Nakata, and S. Shibusawa. Properties and structure of the binary tellurite glasses containing mono- and divalent cations. *Ceramic Society Journal*, 86(7):317–326, 1978.

[22] Beiming Zhou, Charles F. Rapp, John K. Driver, Michael J. Myers, John D. Myers, Jonathan Goldstein, Rich Utano, and Shantanu Gupta. Development of tellurium oxide and lead-bismuth oxide glasses for mid-wave infra-red transmission optics. volume 8626, pages 86261F–86261F–27.

[23] *Tellurite Glasses Handbook: Physical Properties and Data.* CRC Press, Boca Raton, FL, 2002.

[24] J. E. Stanworth. Tellurite glasses. *Nature*, 169(4301):581–582, 1952.

[25] G. Senthil Murugan, Takenobu Suzuki, and Yasutake Ohishi. Tellurite glasses for ultrabroadband fiber raman amplifiers. *Applied Physics Letters*, 86(16):161109, 2005.

[26] Clara Rivero, Kathleen Richardson, Robert Stegeman, George Stegeman, Thierry Cardinal, Evelyne Fargin, Michel Couzi, and Vincent Rodriguez. Quantifying raman gain coefficients in tellurite glasses. *Journal of Non-Crystalline Solids*, 345–346:396–401, 2004.

[27] Xian Feng, Jindan Shi, Martha Segura, Nicolas White, Pradeesh Kannan, Laurent Calvez, Xianghua Zhang, Laurent Brilland, and Wei Loh. Towards water-free tellurite glass fiber for 2-5 μm nonlinear applications. *Fibers*, 1(3):70, 2013.

[28] Rajan Jose, Guanshi Qin, Yusuke Arai, and Yasutake Ohishi. Tailoring of raman gain bandwidth of tellurite glasses for designing gain-flattened fiber raman amplifiers. *Journal of the Optical Society of America B*, 25(3):373–382, 2008.

[29] V. G. Plotnichenko, V. O. Sokolov, V. V. Koltashev, E. M. Dianov, I. A. Grishin, and M. F. Churbanov. Raman band intensities of tellurite glasses. *Optics Letters*, 30(10):1156–1158, 2005.

[30] C. Rivero, R. Stegeman, M. Couzi, D. Talaga, T. Cardinal, K. Richardson, and G. Stegeman. Resolved discrepancies between visible spontaneous raman cross-section and direct near-infrared raman gain measurements in teo2-based glasses. *Opt Express*, 13(12):4759–69, 2005.

[31] M. D. O'Donnell, K. Richardson, R. Stolen, A. B. Seddon, D. Furniss, V. K. Tikhomirov, C. Rivero, M. Ramme, R. Stegeman, G. Stegeman, M. Couzi, and T. Cardinal. Tellurite and fluorotellurite glasses for fiberoptic raman amplifiers: Glass characterization, optical properties, raman gain, preliminary fiberization, and fiber characterization. *Journal of the American Ceramic Society*, 90(5):1448–1457, 2007.

[32] M. D. O'Donnell, K. Richardson, R. Stolen, C. Rivero, T. Cardinal, M. Couzi, D. Furniss, and A. B. Seddon. Raman gain of selected tellurite glasses for ir fibre lasers calculated from spontaneous scattering spectra. *Optical Materials*, 30(6):946–951, 2008.

[33] Takenobu Suzuki, Teruo William Shiosaka, Shohei Miyoshi, and Yasutake Ohishi. Computational and raman studies of phospho-tellurite glasses as ultra-broad raman gain media. *Journal of Non-Crystalline Solids*, 357(14):2702–2707, 2011.

[34] K. Damak, E. Yousef, S. AlFaify, C. Rüssel, and R. Maâlej. Raman, green and infrared emission cross-sectionsof er3+ doped tzppn tellurite glass. *Optical Materials Express*, 4(4):597–612, 2014.

[35] O. Mouawad, C. Strutynski, J. Picot-Clémente, F. Désévédavy, G. Gadret, J. C. Jules, and F. Smektala. Optical aging behaviour naturally induced on as2s3 microstructured optical fibres. *Optical Materials Express*, 4(10):2190–2203, 2014.

[36] Mohamed A. Ettabib, Kamal Hammani, Xian Feng, Mohammad Belal, Jindan Shi, Adonis Bogris, Alexandros Kapsalis, Dimitris Syvridis, David J. Richardson, and Periklis Petropoulos. Highly nonlinear tellurite glass fiber for broadband applications. In *Optical Fiber Communication Conference*, OSA Technical Digest (online), page Tu2K.3. Optical Society of America.

[37] Hiromichi Takebe, Shigeru Pujino, and Kenji Morinaga. Refractive-index dispersion of tellurite glasses in the region from 0.40 to 1.71 um. *Journal of the American Ceramic Society*, 77(9):2455–2457, 1994.

[38] Adrian Carter, Bryce Sampson, and Kanishka Tankala. Thulium-doped fiber forms kilowatt-class laser. *Laser Focus World*, 45(4):51, 2009.

[39] *City of Light: The Story of Fiber Optics*. Oxford University Press, New York, New York, 2005.

[40] Qiuling Chen, Hui Wang, Qingwei Wang, Qiuping Chen, and Yinlei Hao. Modified rod-in-tube for high-na tellurite glass fiber fabrication: materials and technologies. *Applied Optics*, 54(4):946–952, 2015.

[41] A. L. Schawlow and C. H. Townes. Infrared and optical masers. *Physical Review*, 112(6):1940–1949, 1958.

[42] E. Snitzer. Cylindrical dielectric waveguide modes*. *Journal of the Optical Society of America*, 51(5):491–498, 1961.

[43] E. Snitzer and H. Osterberg. Observed dielectric waveguide modes in the visible spectrum*. *Journal of the Optical Society of America*, 51(5):499–505, 1961.

[44] T. H. Maiman. Stimulated optical radiation in ruby. *Nature*, 187(4736):493–494, 1960.

[45] K. C. Kao and G. A. Hockham. Dielectric-fibre surface waveguides for optical frequencies. *Electrical Engineers, Proceedings of the Institution of*, 113(7):1151–1158, 1966.

[46] T. Miya, Y. Terunuma, T. Hosaka, and T. Miyashita. Ultimate low-loss single-mode fibre at 1.55 um. *Electronics Letters*, 15(4):106–108, 1979.

[47] R.J. Mears, L. Reekie, I.M. Jauncey, and D.N. Payne. Low-noise erbium-doped fibre amplifier operating at 1.54 um. *Electronics Letters*, 23(19):1026–1028, 1987.

[48] Jeff Hecht. The clearest glass in the world. *Optics and Photonics News*, 11(10):50–53, 2000.

[49] A. Mawardi and R. Pitchumani. Optical fiber drawing process model using an analytical neck-down profile. *IEEE Photonics Journal*, 2(4):620–629, 2010.

[50] J. C. Knight, T. A. Birks, P. St J. Russell, and D. M. Atkin. All-silica single-mode optical fiber with photonic crystal cladding. *Optics Letters*, 21(19):1547–1549, 1996.

[51] D. Pysz, I. Kujawa, R. Stepien, M. Klimczak, A. Filipkowski, M. Franczyk, L. Kociszewski, J. Buzniak, K. Harasny, and R. Buczynsk. Stack and draw fabrication of soft glass microstructured fiber optics. *Bulletin of the Polish Academy of Sciences Technical Sciences*, 62(4):667–682, 2014.

[52] E. F. Chillcce, C. M. B. Cordeiro, L. C. Barbosa, and C. H. Brito Cruz. Tellurite photonic crystal fiber made by a stack-and-draw technique. *Journal of Non-Crystalline Solids*, 352(32–35):3423–3428, 2006.

[53] J. S. Wang, E. M. Vogel, and E. Snitzer. Tellurite glass: a new candidate for fiber devices. *Optical Materials*, 3(3):187–203, 1994.

[54] Keiron Boyd, Heike Ebendorff-Heidepriem, Tanya M. Monro, and Jesper Munch. Surface tension and viscosity measurement of optical glasses using a scanning co2 laser. *Optical Materials Express*, 2(8):1101–1110, 2012.

[55] R. Stepien, R. Buczynski, D. Pysz, I. Kujawa, and M. Mirkowska. Tellurite glasses for microstructured optical fibers manufacturing. *Photonics Letters of Poland*, 2(1), 2010.

[56] Michael R. Oermann, Heike Ebendorff-Heidepriem, Yahua Li, Tze-Cheung Foo, and Tanya M. Monro. Index matching between passive and active tellurite glasses for use in microstructured fiber lasers: Erbium doped lanthanum-tellurite glass. *Optics Express*, 17(18):15578–15584, 2009.

[57] A. Urich, R. R. J. Maier, Fei Yu, J. C. Knight, D. P. Hand, and J. D. Shephard. Flexible delivery of er:yag radiation at 2.94 um with negative curvature silica glass fibers: a new solution for minimally invasive surgical procedures. *Biomedical Optics Express*, 4(2):193–205, 2013.

[58] Meisong Liao, Chitrarekha Chaudhari, Guanshi Qin, Xin Yan, Takenobu Suzuki, and Yasutake Ohishi. Tellurite microstructure fibers with small hexagonal core for supercontinuum generation. *Optics Express*, 17(14):12174–12182, 2009.

[59] Mariusz Klimczak, Grzegorz Stepniewski, Henry Bookey, Agnieszka Szolno, Ryszard Stepien, Dariusz Pysz, Ajoy Kar, Andrew Waddie, Mohammad R. Taghizadeh, and Ryszard Buczynski. Broadband infrared supercontinuum generation in hexagonal-lattice tellurite photonic crystal fiber with dispersion optimized for pumping near 1560 nm. *Optics Letters*, 38(22):4679–4682, 2013.

[60] X. Feng, T. M. Monro, V. Finazzi, R. C. Moore, K. Frampton, P. Petropoulos, and D. J. Richardson. Extruded singlemode, high-nonlinearity, tellurite glass holey fibre. *Electronics Letters*, 41(15):835–837, 2005.

[61] Xian Feng, Wei H. Loh, Joanne C. Flanagan, Angela Camerlingo, Sonali Dasgupta, Periklis Petropoulos, Peter Horak, Ken E. Frampton, Nicholas M. White, Jonathan H. V. Price, Harvey N. Rutt, and David J. Richardson. Single-mode tellurite glass holey fiber with extremely large mode area for infrared nonlinear applications. *Optics Express*, 16(18):13651–13656, 2008.

[62] I. Savelii, J. C. Jules, G. Gadret, B. Kibler, J. Fatome, M. El-Amraoui, N. Manikandan, X. Zheng, F. Désévédavy, J. M. Dudley, J. Troles, L. Brilland, G. Renversez, and F. Smektala. Suspended core tellurite glass optical fibers for infrared supercontinuum generation. *Optical Materials*, 33(11):1661–1666, 2011.

[63] V. V. Ravi Kanth Kumar, A. K. George, J. C. Knight, and P. St J. Russell. Tellurite photonic crystal fiber. *Optics Express*, 11(20):2641–2645, 2003.

[64] Hidetoshi Onodera, Ikuo Awai, and Jun-ichi Ikenoue. Refractive-index measurement of bulk materials: prism coupling method. *Applied Optics*, 22(8):1194–1197, 1983.

[65] Y. Ohishi, G. Qin, M. Liao, X. Yan, and T. Suzuki. Recent progress in tellurite fibers. In *Optical Fiber Communication (OFC), collocated National Fiber Optic Engineers Conference, 2010 Conference on (OFC/NFOEC)*, pages 1–3.

[66] Scott Diddams and Jean-Claude Diels. Dispersion measurements with white-light interferometry. *Journal of the Optical Society of America B*, 13(6):1120–1129, 1996.

[67] *Supercontinuum Generation in Optical Fibers*. Cambridge University Press, New York, 2010.

[68] Inna Savelii, Frederic Desevedavy, Jean-Charles Jules, Gregory Gadret, Julien Fatome, Bertrand Kibler, Hiroyasu Kawashima, Yasutake Ohishi, and Frederic Smektala. Management of oh absorption in tellurite optical fibers and related supercontinuum generation. *Optical Materials*, 35(8):1595–1599, 2013.

[69] Heike Ebendorff-Heidepriem, Kevin Kuan, Michael R. Oermann, Kenton Knight, and Tanya M. Monro. Extruded tellurite glass and fibers with low oh content for mid-infrared applications. *Optical Materials Express*, 2(4):432–442, 2012.

[70] Quentin Coulombier, Laurent Brilland, Patrick Houizot, Thierry Chartier, Thanh Nam N'Guyen, Frédéric Smektala, Gilles Renversez, Achille Monteville, David Méchin, Thierry Pain, Hervé Orain, Jean-Christophe Sangleboeuf, and Johann Trolès. Casting method for producing low-loss chalcogenide microstructured optical fibers. *Optics Express*, 18(9):9107–9112, 2010.

[71] M. D. O'Donnell, D. Furniss, V. K. Tikhomirov, and A. B. Seddon. Low loss infrared fluorotellurite optical fibre. *Physics and Chemistry of Glasses - European Journal of Glass Science andTechnology Part B*, 47(2):121–126, 2006.

[72] Aoxiang Lin, Aleksandr Ryasnyanskiy, and Jean Toulouse. Fabrication and characterization of a water-free mid-infrared fluorotellurite glass. *Optics Letters*, 36(5):740–742, 2011.